UNIVERSITÄT GREIFSWALD
Wissen lockt. Seit 1456

Particle Simulations of Electrons in Paul Traps

by

Edith Victoria Hausten

A thesis presented for the degree of
Master of Science

1. Supervisor: Prof. Dr. Ralf Schneider
2. Supervisor: Prof. Dr. Hartmut Häffner

Institute of Physics
Faculty of Mathematics and Natural Sciences
University of Greifswald

Greifswald, December 2022

Contents

1. Motivation

1.1. Quantum Computation

Over the last decades, classical processors have continuously grown more powerful and more compact. However, this process is already starting to saturate due to simple physical limitations. As integrated circuits are growing ever smaller (nm range), they are approaching a regime where classical laws of physics do no longer hold, but quantum mechanical effects start dominating. Meanwhile, research on quantum computation has widely expanded with exciting achievements. A quantum computer is a device that processes information based on the laws of quantum mechanics. In contrast to a classical computer, that works based on macroscopic electronic states, a quantum computer acts on quantum states. Information is stored in qubits with states $|0\rangle$ and $|1\rangle$, in analogy to the binary states 0 and 1 of a classical bit. There are several different approaches how to realize a quantum computer. The two-state system can be represented by the direction of the electric current in a superconducting circuit, by two different energy levels of an ion or by the spin states of an electron.

In addition to overcome the before-mentioned physical length scale limitations, the realisation of a quantum device also promises very fast speedups in solving certain computational problems such as the Traveling Salesmen Problem or the factorisation of large numbers with Shor's algorithm. Quantum devices are making use of the probabilistic behavior of quantum mechanic. Before a measurement, the state of a qubit is not purely $|0\rangle$ nor $|1\rangle$ but a superposition $c_0 |0\rangle + c_1 |1\rangle$, with $c_0, c_1 \in \mathbb{C}$ and $|c_0|^2 + |c_1|^2 = 1$. This implies that the theoretical possibility exists to process exponentially more data at the same time compared with a classical computer. The potential applications of quantum computers reach from cryptography to search problems in large databases and simulations of complex quantum and non-quantum systems, to name only a few.

1.2. The Electron Qubit

One of the most advanced and promising candidates for the experimental realisation of a qubit is to use trapped ions stored in vacuum Paul traps. In analogy, it is possible to trap electrons in Paul traps, even though this is more challenging due to the electrons' lighter mass and higher velocity. Recent efforts at the University of California Berkeley were successful. In [1] the research group of Prof. Häffner proposes a prototype design of a trapped electron quantum computing device. A potential electron qubit conserves the advantages of ion qubits, but overcomes at the same time a few of the ion qubit's weaknesses. In contrary to superconducting wire qubits, ions and electrons are perfectly interchangeable particles, having for sure the same physical properties. This is quite difficult to achieve for artificially manufactured qubits, such as wires. Having only two possible spin states, the electron provides a perfect two-level system, eliminating possible information leakage to states outside of the logical space. Trapped ion qubits are cooled and manipulated using laser light to induce optical transitions. Even though these control processes are well understood and working reliably, building a large scale quantum computer with such qubits requires optical access to the system, which is a very challenging engineering task. This issue does not exist for electron qubits that are entirely controlled without complicated optics. Cooling and detection can be achieved by using a cryogenic tank circuit coupled to the electron dynamics. Manipulation of single qubits can be realised by applying microwave pulses near the Zeeman resonance. Also two-qubit gates can be realised using constant or oscillating magnetic field gradients, acting on two electron qubits that are coupled to each other. Finally, due to the lighter mass and higher velocity, electrons are trapped at higher secular frequencies compared to ions, allowing faster gate times for multi-qubit operation and transport.

1.3. Research Question

At the moment, trapped electron quantum computation is still a very young field of research with many questions not yet answered. While trapping electrons in Paul traps has already been demonstrated, important milestones such as motional cooling and the formation of Coulomb crystals has not yet been observed in Paul traps. Coulomb crystals form in an ideal trapping potential for sufficiently low energies, but it is not yet clear if they are stable under real experimental conditions. Therefore, the central research topic of this thesis is the **numerical investigation of the dynamics and stability of electrons in a Paul trap**. To study this issue for realistic conditions, the most important physical processes are modelled in a particle simulation. This will help building up a theoretical basis for current and future trapped electron experiments. The motion of electrons is studied in the anharmonic potential of a real Paul trap, currently in use at the University of California, Berkeley.

After this motivating chapter, the basic physics for answering the research question of this thesis is shortly introduced: the dynamics in Paul traps, the properties of anharmonic trapping potentials, the formation of Coulomb crystals as well as the resistive cooling process and the Johnson Nyquist noise. After that, the simulated trap and its potential are described in detail. The potential is found numerically with a finite element method. Also, the numerical integration method used in this work is discussed. Then, the results of the particle simulations are presented for the realistic trap potential. Simulations with an approximated trapping potential without anharmonicities are used as reference. This comparison allows to identify the influence of the anharmonicites, present in the realistic trap potential, on the electron dynamics. At first, the traps motional frequencies are calculated. A model for simulating resistive cooling in axial direction and the corresponding Johnson Nyquist noise, originating from the tank circuit, is introduced. Cooling times and efficiency are discussed as well as the coupling of the axial and radial motional modes due to anharmonicities and Coulomb interaction between electrons. The formation and stability of Coulomb crystals in the anharmonic and noisy system is discussed for the simplest possible crystal configuration, namely the two-electron structure. Studies on two-electron structures are a good starting point for future research on larger structures. In addition, they are relevant for the realisation of two-electron qubits. This thesis ends with a summary of the most important results with respect to the research question, along with an outlook on possible future research beyond this thesis.

2. Basic Physics

This chapter presents the basic physics needed to understand the processes of trapping and manipulating electrons in Paul traps.

2.1. Trapping Electrons with Paul Traps

Paul traps, also known as quadrupole traps or radio frequency traps, were invented by the german physicist Wolfgang Paul, who was awarded with the Nobel Price of Physics in 1989 for this work. They are mainly used for mass spectrometry experiments and ion trapping, even though they are in principle suitable for trapping any charged particle, including electrons, using time-varying electric fields.

2.1.1. General Operation Principle

According to Earnshaw's theorem [2], it is impossible to trap charged particles in three dimensions by using purely static electric fields. This can be easily demonstrated by considering a three dimensional, harmonic electric potential in directions x, y, z

$$\Phi = \alpha x^2 + \beta y^2 + \gamma z^2, \tag{2.1}$$

$\alpha, \beta, \gamma \in \mathbb{R}$, with a resulting electric field

$$\mathbf{E} = -\nabla\Phi = -2\begin{pmatrix}\alpha x\\ \beta y\\ \gamma z\end{pmatrix}. \tag{2.2}$$

Applying Gauss' law in vacuum,

$$\nabla\mathbf{E} = -2(\alpha+\beta+\gamma) = 0, \tag{2.3}$$

implies that for a nonzero potential at least one of the coefficients α, β or γ must be negative to produce a repulsive potential in at least one direction. Therefore, Paul traps use time-varying electric fields in the radio frequency range that create an average confining force. To keep the charged particle stored in the trap, the switching rate must be faster than the particle's escape from the trap. For trapped electron experiments, the switching frequency has to be significantly higher than for trapped ions, due to the electrons smaller mass and larger velocity. Earnshaw's principle can be interpreted as a fast rotating saddle potential and is illustrated in figure 2.1.

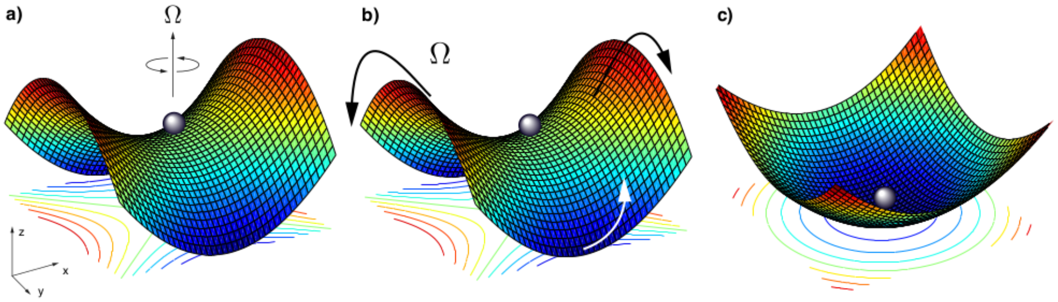

Figure 2.1.: Visualisation of a) a particle in a rotating saddle potential with rotation frequency Ω, b) a flapping potential with flapping frequency Ω and c) the effective trapping potential that results from both scenarios [3].

2.1.2. Linear Paul Traps

In linear Paul traps a three dimensional trapping potential can be realised with an electrode configuration consisting of six electrodes. Four RF-electrodes are aligned around an axis as shown in figure 2.2. A periodically alternating AC voltage is applied to the configuration.

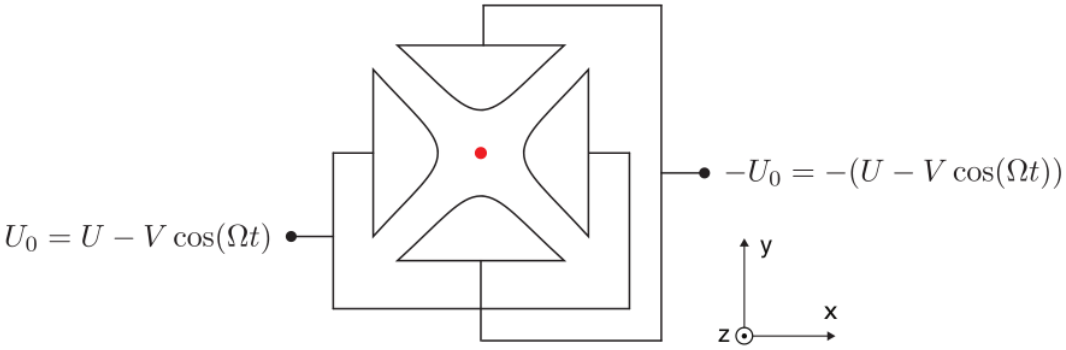

Figure 2.2.: Schematic RF-electrode configuration of a Paul trap. The voltage applied to the electrodes is changing harmonically within the range of $-U_0$ and U_0. Same voltages are applied to electrodes facing each other [3].

The pairs of electrodes facing each other are held at same voltages: the first pair of electrodes (left and right electrodes in figure 2.2) is kept at U_0, while the second pair of electrodes (upper and lower electrodes in figure 2.2) is kept at $-U_0$. Here

$$U_0 = U - V\cos(\Omega t) \tag{2.4}$$

refers to a time-dependent AC voltage V, driven at frequency Ω, with a constant offset voltage U that is time-independent. The RF-electrodes provide a switching saddle potential as discussed above and thus allow trapping of a charged particle in two dimensions x- and y. To realise trapping in three directions, an additional pair of DC-electrodes is required to provide a static confining potential in z direction. In the following the x and y directions are also referred to as the radial directions while the z direction is called the axial direction.

In a lowest order approximation, the above discussed electrode configuration provides the trapping potential

$$\begin{aligned}
\Phi^{harm.} &= \Phi_{RF}^{harm.} + \Phi_{DC}^{harm.} && (2.5)\\
&= V\cos(\Omega t)\left(\frac{x^2-y^2}{r_0^2}\right) + \kappa U\left(\frac{2z^2-x^2-y^2}{2z_0^2}\right), && (2.6)
\end{aligned}$$

where the constants r_0, z_0 and κ are determined by the trap geometry and size.

2.1.3. Mathieu Equations and Motional Frequencies

The force $\mathbf{F}$ of the trapping potential, acting on a charged particle of mass m and charge q, is $\mathbf{F} = -q\nabla\Phi$, which gives the equation of motion

$$m\ddot{\mathbf{r}} = -q\nabla\Phi, \tag{2.7}$$

with the position $\mathbf{r}^{\mathsf{T}} = (x, y, z)$ and acceleration $\ddot{\mathbf{r}}$. It is convenient to define the following parameters:

$$\begin{aligned}
a_x = a_y = -\frac{1}{2}a_z &= -\frac{4q\kappa U}{mz_0^2\Omega^2}\,, && (2.8)\\
q_x = -q_y &= -\frac{4qV}{mr_0^2\Omega^2}\,, && (2.9)\\
q_z &= 0\,, && (2.10)\\
\tau &= \frac{1}{2}\Omega t\,, && (2.11)
\end{aligned}$$

and to rewrite the equation of motion as

$$0 = \frac{d^2 r_u}{d\tau^2} + (a_u - 2q_u \cos(2\tau))r_u, \tag{2.12}$$

with $u \in \{x, y, z\}$. For the axial direction, $u = z$, equation 2.12 represents simply a harmonic oscillator. In the radial directions $u = x, y$, the equations of motion 2.12 have the form of Mathieu-Equations, which are special cases of the Hill-Equation. The Mathieu-Equation is solved with the ansatz

$$u(\tau) = Ae^{i\beta_u \tau} \sum_n C_{2n} e^{i2n\tau} + e^{-i\beta_u \tau} \sum_n C_{-2n} e^{-i2n\tau}, \tag{2.13}$$

with the stability parameter $\beta_u = \sqrt{a_u + \frac{q_u^2}{2}}$, as described in [4]. The resulting radial particle trajectories $r_{x,y}(t)$ can be thought of as harmonic oscillations of the mean position $\langle r_{x,y}(t) \rangle$ with additional small oscillating deviations from the mean position $\delta r_{x,y}(t)$

$$r_{x,y}(t) = \langle r_{x,y}(t) \rangle + \delta r_{x,y}(t). \tag{2.14}$$

The oscillation of the mean position is called secular motion or macro motion while the small deviation of the trajectories is called micro motion [5].

The stability of the particle's motion and trapping depends on the parameters a_u and q_u. This relation can be visualised in a Mathieu stability diagram as in figure 2.3. The r-stable (i.e. radially stable, meaning x- and y-stable) and z-stable regions are depicted for an ideal linear quadrupole ion trap, as a function of the parameters a_u and q_u. Three-dimensional trapping is only possible for regions that are both r- and z-stable, in other words r-z-stable.

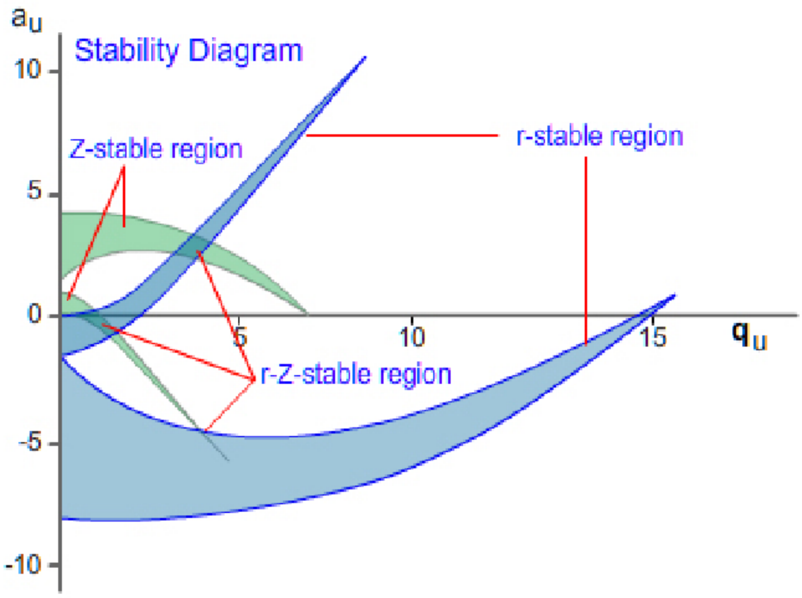

Figure 2.3.: The Mathieu stability diagram shows stable trapping regions for an ideal quadrupole ion trap as a function of the parameters a_u and q_u [6].

The rest of this section is again following the elaborations in [4]. Usually, Paul traps are operated in a regime where $|a_u| \ll 1$ and $q_u^2 \ll 1$. This justifies a first order approximation for the particle trajectory, giving

$$u(t) \approx A\cos(\omega_{u,sec}\, t)\left(1 - \frac{q_u}{2}\cos(\Omega t)\right). \tag{2.15}$$

The first term provides an oscillation with frequency

$$\omega_{u,sec} = \frac{\Omega}{2}\beta_u = \frac{\Omega}{2}\sqrt{a_u + \frac{q_u^2}{2}}. \tag{2.16}$$

The second term has a much smaller amplitude and can be rewritten as

$$\cos(\omega_{u,sec}t)\cos(\Omega t) = \cos\big((\Omega + \omega_{u,sec})t\big) + \cos\big((\Omega - \omega_{u,sec})t\big), \tag{2.17}$$

showing that it oscillates with the frequency of the micro motion Ω plus and minus the secular frequency $\omega_{u,sec}$. These frequencies are called the first two sidebands of the motion. From equation 2.16 the axial secular frequency can be obtained as

$$\omega_{z,sec} = \frac{\Omega}{2}\sqrt{a_z} = \sqrt{\frac{2qU\kappa}{mz_0^2}}. \tag{2.18}$$

In the radial directions, the static DC-potential should ideally have only a very small impact compared with the RF-potential ($a_{x,y} \ll q_{x,y}^2$). We can therefore assume $a_{x,y} \approx 0$, to find the radial secular frequencies

$$\omega_{x,y,sec} = \frac{\Omega}{2}\frac{q_{x,y}}{\sqrt{2}} = \frac{\sqrt{2}qV}{m\Omega r_0^2}. \tag{2.19}$$

Hence, due to the much smaller electron mass and higher velocity, the secular frequencies of trapped electrons are much higher than those of trapped ions.

2.2. Planar Traps and Impact of Anharmonicities

A perfect quadrupole trapping potential as introduced before is only achievable in linear Paul traps with perfectly hyperbolically shaped electrodes. In practice, it is rather common to use planar segmented trap geometries instead of classical linear Paul traps. Planar Paul traps consist of an RF- and DC-electrode configuration that lies completely within one plane. The charged particle is trapped above this plane as shown in figure 2.4. Planar traps come along with a couple of big advantages compared with the classical linear traps. Standardized and efficient micro-fabrication methods can be used for trap fabrication, such as photolithography and metal evaporation deposition. Planar traps are also popular for their good scalability. It is possible to fabricate very compact traps, in particular with multiple trapping zones and shuttling zones to carry the charged particles in between different zones.

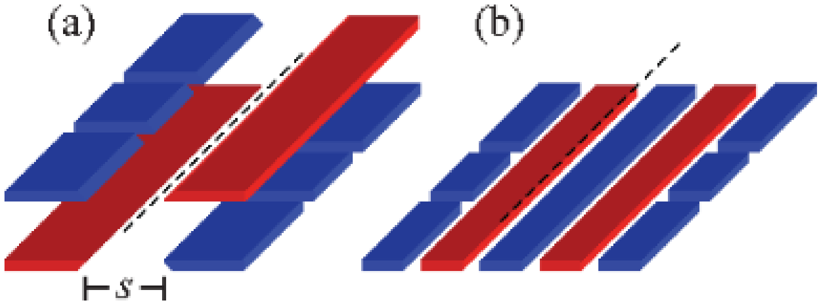

Figure 2.4.: Comparison of a) a linear Paul trap and b) a planar ion trap by [7]. The dashed line represents the trapping axis. The RF-electrodes are colored in red and realise the radial confinement. The DC-electrodes are colored in blue and allow axial confinement.

For quantum computation, such a system is highly favorable. The main object of investigation in this thesis is a 3-layer planar Paul trap, designed by the Trapped Ions Group at the University of Berkeley. It is described in more detail in section 3.1.

There is also a disadvantage of such planar traps. The electrode configuration is usually more complex and consists of larger numbers of electrodes compared with idealized Paul traps. This results in a more complicated trapping potential which can be calculated only numerically. In particular, the potential created by planar traps is not simply a quadrupole potential, but a linear combination of infinitely many multipoles $\mathbf{r}^2$, $\mathbf{r}^3$, $\mathbf{r}^4$, ... The deviation of the trapping potential from an ideal, pure quadrupole potential is called anharmonicity. The anharmonicity of an electron Paul trap affects its motional frequencies, cooling and readout and it is generally favorable to minimize its impact. A description of the influence of anharmonicities on various aspects of electron trapping can be found in [8]. The effect of anharmonicities is stronger at positions further away from the trap center. Therefore, they are even more relevant for trapped electron experiments compared with trapped ion experiments. Due to their smaller mass electrons experience regions of the trapping potential with stronger anharmonic terms. In the following is discussed how an anharmonic Paul trap potential can be described as an expansion in spherical harmonics.

Laplace's equation must hold for the trapping potential, which reads in spherical coordinates (r, θ, φ)

$$\Phi = \frac{1}{r^2}\frac{\partial}{\partial r}\left(r^2 \frac{\partial \Phi}{\partial r}\right) + \frac{1}{r^2 \sin{(\theta)}}\frac{\partial}{\partial \theta}\left(\sin{(\theta)}\frac{\partial \Phi}{\partial \theta}\right) + \frac{1}{r^2 \sin^2(\theta)}\frac{\partial^2 \Phi}{\partial \varphi^2} = 0, \tag{2.20}$$

and which is solved by the method of separating variables into a radial part $R(r)$ and angular parts $\Theta(\theta)$, $\phi(\varphi)$

$$\Phi(r, \theta, \phi) = R(r)\Theta(\theta)\phi(\varphi). \tag{2.21}$$

This expression can be expanded in terms of spherical harmonics as it is shown in textbooks as [9], giving

$$\Phi(r, \theta, \varphi) = \sum_{l=0}^{\infty} \sum_{m=-l}^{l} (A_{lm} r^l + B_{lm} r^{-l-1}) Y_{lm}(\theta, \varphi). \tag{2.22}$$

Y_{lm} are the spherical harmonics

$$Y_{lm}(\theta, \varphi) = \sqrt{\frac{(2l+1)(l-m)!}{4\pi(l+m)!}}\, P_l^m(\cos\theta) e^{im\varphi}, \tag{2.23}$$

with the associated Legendre functions

$$P_l^m(\cos\theta) = (-1)^m (\sin\theta)^m \frac{d^m}{d(\cos\theta)^m} \big(P_l(\cos\theta)\big), \tag{2.24}$$

with the Legendre polynomials $P_l(\cos\theta)$ following Rodrigues' Formula

$$P_l(x\cos\theta) = \frac{1}{2^l l!} \frac{d^l}{d(\cos\theta)^l} \big((\cos\theta)^2 - 1\big)^l. \tag{2.25}$$

In this notation A_{lm} and B_{lm} are the expansion constants. It turns out that $B_{lm} = 0$, $\forall l, m$, since the second term $B_{lm} r^{-l-1}$ diverges for nonzero constants B_{lm} at the trapping axis $r = 0$. The expansion thus simplifies to

$$\Phi(r, \theta, \varphi) = \sum_{l=0}^{\infty} \sum_{m=-l}^{l} A_{lm} r^l Y_{lm}(\theta, \varphi). \tag{2.26}$$

The spherical harmonics Y_{lm} form a complete set of orthogonal functions. They satisfy the orthogonality property

$$\int d\Omega Y^*_{l'm'}(\theta, \varphi) Y_{lm}(\theta, \varphi) = \delta_{ll'} \delta_{mm'}, \tag{2.27}$$

with the complex conjugate $Y^*_{lm}(\theta, \varphi) = (-1)^m Y_{l,-m}(\theta, \varphi)$. This property allows to write down a formula for the expansion coefficients

$$A_{lm} = \int d\Omega Y^*_{lm}(\theta, \varphi) \Phi(r, \theta, \varphi). \tag{2.28}$$

The potential expansion 2.26 can be rewritten in Cartesian coordinates by applying the standard back transformation. A transformation to an expansion with single index basis functions and coefficients is obtained by applying a mapping proposed by [3]. The single index basis functions Y_j are obtained by

$$Y_j = \begin{cases} r^{l_j} Y_{\ell_j,0} & \text{if } m_j = 0 \\ \frac{1}{\sqrt{2}} r^{l_j} \left((-1)^{m_j} Y_{\ell_j,m_j} + Y_{\ell_j,-m_j} \right) & \text{if } m_j > 0 \\ \frac{i}{\sqrt{2}} r^{l_j} \left(Y_{\ell_j,m_j} - (-1)^{m_j} Y_{\ell_j,-m_j} \right) & \text{if } m_j < 0 \end{cases} , \tag{2.29}$$

and the corresponding single index coefficients M_j by

$$M_j = \begin{cases} A_{\ell_j,0} & \text{if } m_j = 0 \\ \frac{1}{\sqrt{2}}\left((-1)^{m_j} A_{\ell_j,m_j} + A_{\ell_j,-m_j}\right) & \text{if } m_j > 0 \\ \frac{-i}{\sqrt{2}}\left(A_{\ell_j,m_j} - (-1)^{m_j} A_{\ell_j,-m,}\right) & \text{if } m_j < 0 \end{cases} \quad . \tag{2.30}$$

Every index j in the single index notation corresponds to two indices l_j and m_j in the two-index notation, as demonstrated below up to $l = 2$

$$\begin{pmatrix} j \\ 1 \\ 2 \\ 3 \\ 4 \\ 5 \\ 6 \\ 7 \\ 8 \\ 9 \end{pmatrix} \rightarrow \begin{pmatrix} \ell_j & m_j \\ 0 & 0 \\ 1 & -1 \\ 1 & 0 \\ 1 & 1 \\ 2 & -2 \\ 2 & -1 \\ 2 & 0 \\ 2 & 1 \\ 2 & 2 \end{pmatrix} . \tag{2.31}$$

We end up with a simple single index version of the expansion 2.26 for the trapping potential in Cartesian coordinates that is used later in this thesis to describe the realistic potential of the experimental Paul trap:

$$\Phi(x, y, z) = \sum_{j=1}^{\infty} M_j Y_j(x, y, z). \tag{2.32}$$

2.3. Coulomb Crystals

Multiple charged particles trapped in the same potential can be cooled down to low energies to form Coulomb crystals. The thermal motion of the particles is cooled down into a quasi-stationary state where the Coulomb repulsion between the particles and the trapping potential pushing the electrons back to the trap center are balancing each other. Having a total number of N particles of charges q_i at positions $\mathbf{r}_i$, the Coulomb force acting on one of them with charge q at position $\mathbf{r}$ is

$$\mathbf{F}_{Coul}(\mathbf{r}) = \frac{q}{4\pi\epsilon_0} \sum_{i=1}^{N} q_i \frac{\mathbf{r} - \mathbf{r}_i}{|\mathbf{r} - \mathbf{r}_i|^3}, \tag{2.33}$$

where ϵ_0 is the vacuum permittivity. There has been a lot of research on ions in Paul traps, where large Coulomb crystals of up to several hundreds of ions can be formed. Figure 2.5 shows an experiment by [10] on ion crystals, changing shape as the axial potential strength is varied.

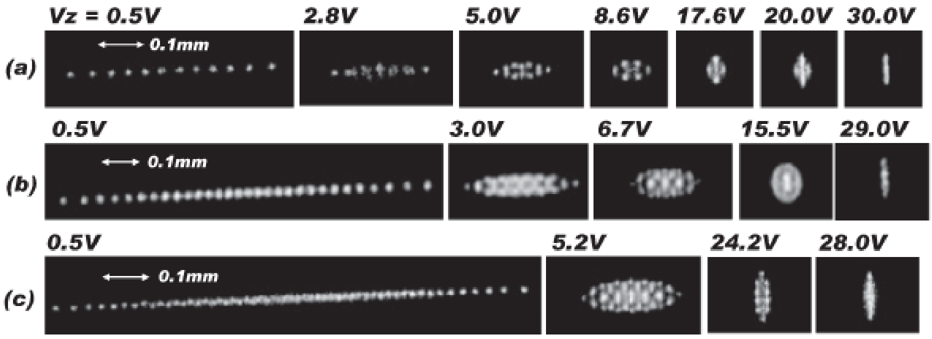

Figure 2.5.: Coulomb crystals in Paul traps, consisting of a) $N = 12$, b) $N = 30$ and c) $N = 55$ ions. The shape of the Coulomb crystal is changing with the strength of the axial trapping potential [10].

This thesis focuses on the investigation of the simplest form of electron Coulomb crystals, consisting of only two electrons. The two electrons align along the weakest trapping axis, which is the z-axis, forming a one-dimensional crystal. The presence of multiple charged particles moving freely, i.e. in a 'gas state' within the same trap, causes RF-heating.

Within this heating mechanism, energy is transferred from the RF-field to the trapped ions or electrons. The process is described in detail in many publications such as [11] and [12]. It results from Coulomb collisions between the particles in the alternating RF-field. The RF-force can intensify Coulomb collisions and this way add energy to the system [12]. The crystal state is extremely advantageous, as it protects the particles from that heating mechanism by preventing strong Coulomb collisions [11]. The motion of a two-electron crystal has six degrees of freedom: three center-of-mass modes that follow the regular secular frequencies ω_{ax} and ω_{rad} of the trap and three vibration modes, i.e. the motion relative to the center-of-mass. The relative motion in radial directions is referred to as 'zigzag' or 'rocking' mode and the axial relative motion as 'stretch' or 'breathing' mode. Zigzag and stretch modes do not show the traps regular secular frequencies but oscillate at

$$\omega_{zigzag} = \sqrt{\omega_{rad}^2 - \omega_{ax}^2}, \tag{2.34}$$

$$\omega_{stretch} = \sqrt{3}\,\omega_{ax}, \tag{2.35}$$

according to [13]. All motional modes have to remain bounded for a stable crystal state. While the stability of the center-of-mass motion is achieved for the stable trapping zones of the Mathieu diagram, the stability of the relative motion is less obvious. There exist stable trapping regions in the Mathieu diagram that are 'crystal free', meaning that no crystal state will form even for low energies [14].

Indeed, the stability of Coulomb crystals is affected by several factors. Melting can be induced by collisions with residual background gas as well as by noise. While cooling to a low energy level is necessary for crystallisation, a too strong damping force can also lead to a melting processes in adverse configurations, since the Mathieu stability regions are modified by the additional force [14]. Crystal stability is a very complex topic and this thesis investigates the dynamics and stability of two-electron crystals in terms of temperature and noise. A better understanding is crucial for the development of two-electron qubits for quantum processing.

2.4. Resistive Cooling and Johnson Nyquist Noise

In order to form Coulomb crystals and to be used for quantum gate operations, ions or electrons that serve as qubits need to be cooled down close to their motional ground state. In order to achieve this, effective cooling mechanisms are necessary. They are also crucial for overcoming common heating mechanisms within the trap, such as electrical surface field noise and RF-heating, as explained in greater detail in [12]. For trapped ions, there exist several common methods such as Doppler- or sideband-cooling, that rely on optical excitation of the ion's electronic states. These methods are therefore not an option for electron cooling. Instead, the electron motion can be damped using a tank circuit. The method was proposed by [1] and is depicted in figure 2.6. Its feasibility has already been demonstrated in Penning trap experiments [15]. The electron with elementary charge e oscillates in axial direction with velocity $\dot{z}$ (in the figure denoted as v) within the electrodes. The tank circuit can be described approximately as a plate capacitor with effective distance d_{eff}, connected to a resistor with impedance Z and real part $R = \mathrm{Re}(Z)$. The electron's movement induces a current $I_{ind} = \frac{e\dot{z}}{d_{eff}}$ within the tank circuit, that can be used for electron detection and generates a potential difference $U_{ind} = RI_{ind}$ on the plate capacitor. The resulting damping force $F_{damp} = -\frac{eU_{ind}}{d_{eff}}$ on the electron opposes its motion. Inserting the above expression for the induced current, the damping force reads

$$F_{damp} = -\left(\frac{e}{d_{eff}}\right)^2 R\dot{z}. \tag{2.36}$$

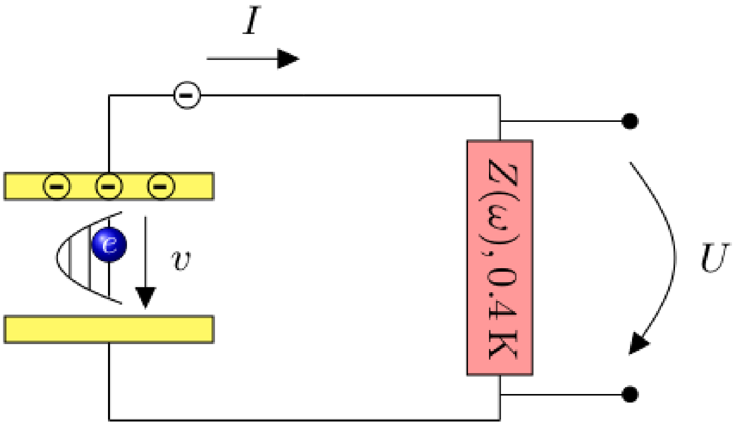

Figure 2.6.: Illustration of the cooling circuit of the electron trap prototype by [1].

However, the Johnson Nyquist noise, originating from the Brownian particle motion within the resistor at nonzero temperature T_{res}, is equally transmitted to the electron's motion. The noise can be thought of as an additional fluctuating voltage $U_{noise}(t)$, applied to the capacitor plates. The Johnson Nyquist noise amplitude is Gaussian distributed with mean $\langle U_{noise} \rangle = 0$ and variance $\langle U_{noise}^2 \rangle = 4k_B T_{res} R \Delta f$, where k_B is the Boltzmann constant and Δf is the bandwidth of the frequency f, over which the noise is measured. In summary, the total force acting on the electron in the cooling circuit reads

$$\begin{aligned} F_{circuit}(t) &= F_{damp}(t) + F_{noise}(t) && (2.37) \\ &= -\left(\frac{e}{d_{eff}}\right)^2 R\dot{z}(t) - \frac{e}{d_{eff}} U_{noise}(t). && (2.38) \end{aligned}$$

The tank circuit is cooling the electron's motion as long as it is above the Johnson Nyquist noise level of the resistor. The tank circuit is kept at cryogenic temperatures to lower the noise level as much as possible. In the equilibrium state, the electron's motion is dominated by the noise and its energy follows a Boltzmann distribution with the temperature equal to the resistors temperature T_{res}. This has been experimentally shown for trapped ions by [15].

In $1D$ the Boltzmann distribution in terms of energy E at temperature T takes the form

$$f_E(E) = \sqrt{\frac{1}{\pi E k_B T}} \exp\left(-\frac{E}{k_B T}\right). \tag{2.39}$$

The ergodic hypothesis holds for the system, meaning that the time average of a single particle is equivalent to the average over an ensemble of many particles at a fixed time. This observation justifies the determination of the electron's 'temperature' T_{eq} in the equilibrium state. The equilibrium temperature in axial direction $T_{eq,ax}$ can be calculated by taking the time average of the electron's total axial energy $\langle E_{ax} \rangle$

$$T_{eq,ax} = \frac{\pi}{k_B} \langle E_{ax} \rangle = T_{res}. \tag{2.40}$$

This results from the $1D$ temperature definition for free gases, where the mean speed is $\langle |v| \rangle = \sqrt{\frac{2k_B T}{\pi m}}$ and the mean kinetic energy is $\langle E \rangle = \frac{1}{2} m \langle |v| \rangle^2 = \frac{k_B T}{\pi}$. In the experiment, the electron's kinetic energy in axial direction can be determined by the strength of the induced current on the pic-up-electrodes. The potential energy is not easily accessible but the total energy can be estimated from the kinetic energy by making use of the Virial theorem. It states that for a conservative potential of order k, the relation between kinetic and potential energy is $\langle E_{kin} \rangle = \frac{k}{2} \langle E_{pot} \rangle$. Assuming an ideal quadratic potential where $k = 2$, we find that $\langle E_{kin} \rangle = \langle E_{pot} \rangle$ and thus $\langle E \rangle = 2 \langle E_{kin} \rangle$.

The autocorrelation function

$$c_{EE}(t, t + \tau) = \langle E(t) E(t + \tau) \rangle \tag{2.41}$$

of the fluctuating energy follows a decaying exponential function with time constant τ_{decay}. This time constant is equal to the cooling time constant of the tank circuit [15].

In an ideal quadrupole potential, the motion in x-, y-, and z directions are independent as long as there is only a single electron present in the trap. With multiple electrons in the same trap, the directions are coupled to each other via the Coulomb interaction, which is inverse proportional to the total distance of the electrons. In an experimental trap, the anharmonicities provide another coupling between the directions, since they contain mixed terms xy, xyz^2, etc. The coupling leads to an energy exchange between the directions. This means that cooling the axial direction could result not only in a lower axial energy but also in a lower radial energy. One goal of this thesis is to determine the coupling strength between axial and radial motion due to anharmonicities and Coulomb interaction. A possible approach is to observe the time constant of the cooling of the radial motion via cooling of the axial motion. In the case of multiple trapped electrons, the coupling strength varies significantly, depending on whether the electrons are in a crystal or gas state.

For a two electron system coupled to a cooling tank circuit, the circuit is impacting the center-of-mass motion of both electrons, but has no direct effect on their relative motion. It is thus impossible to damp the electrons' relative motion directly via a resistive cooling method. The energy stored in the relative motion can prevent the system from freezing into a Coulomb crystal or can lower the stability and lifetime of an already existing Coulomb crystal. Therefore, it is necessary to understand, whether the relative motion can be cooled indirectly via coupling effects between the different motional modes. This question is investigated later in this thesis.

3. Simulation

The basic physics of electron trapping in Paul traps has been discussed in the previous chapter. This chapter will concentrate on the properties of the specific Paul trap that is investigated in this thesis. Special focus is laid on the trapping potential and how it is calculated. Also, the Velocity Verlet integration is introduced, as it is the key element of the particle simulations, performed within this thesis.

3.1. Simulated Trap

The particular electron trap that is investigated in this thesis is a planar three layer Paul trap. It is currently in use for trapped electron experiments in the Trapped Ions Group of Prof. Häffner at the University of California, Berkeley. The trap is designed to trap electrons at motional frequencies of $\omega_{rad} = 2\pi \cdot 300$ MHz and $\omega_{ax} = 2\pi \cdot 30$ MHz and is operated at the driving frequency $\Omega = 2\pi \cdot 1.6$ GHz.

The trapping potential for the particle simulations is determined using the commercial software Ansys Electronics. This software can be used to calculate the potential of any given electrode configuration on a $3D$ grid, using a finite element algorithm (FEM). This is carried out for both the DC- and RF-electrodes separately on a cubic grid of size 300 μm × 300 μm × 300 μm, with a step size of 1 μm, centered around the trap center. For license reasons, the FEM calculations could only be carried out on a regular desktop computer which limited the grid resolution to 1 μm. The potential data obtained by the Ansys algorithm is then used to determine the coefficients M_j of the expansion 2.32 up to order $j = 4$ by a least-squares fit for the DC- and RF-potential separately. Due to the linear relation of applied electrode voltage and potential strength, it is sufficient and reasonable to execute the Ansys FEM algorithm only once for the electrode configuration with 1 V applied to each electrode and scale the resulting expansion coefficients M_j found by the fit afterwards, according to the voltages that are actually applied in the experiment.

Then, the full realistic potential is found by adding both the DC- and RF-components and multiplying the RF-component by a cosine function with driving frequency

$$\Phi^{real.}(x,y,z,t) = \Phi^{real.}_{DC}(x,y,z) + \Phi^{real.}_{RF}(x,y,z,t) \tag{3.1}$$

$$= \sum_{j=1}^{4} \big(M_{j,DC} + M_{j,RF}\cos(\Omega t)\big) Y_j(x,y,z). \tag{3.2}$$

The basis functions Y_j of the expansion up to $j = 6$, as well as the DC- and RF- expansion coefficients $M_{j,DC}$ and $M_{j,RF}$ up to $j = 4$ can be found in the appendix at A.1 and A.2. The order of the expansion has an impact on the values of the expansion coefficients M_j. Fitting the same potential data to an expansion up to order $j = 4$ obtains not only less but also different coefficients than fitting it to an expansion up to order $j = 6$.

Figure 3.1 shows a cross section of the raw data at $z = 0$ for the RF-potential. The potential in different cuts in x, y, z, calculated by Ansys for voltages 1 V on the electrodes, is depicted in figure 3.2. Also shown are the least-square fits to the expansion formula.

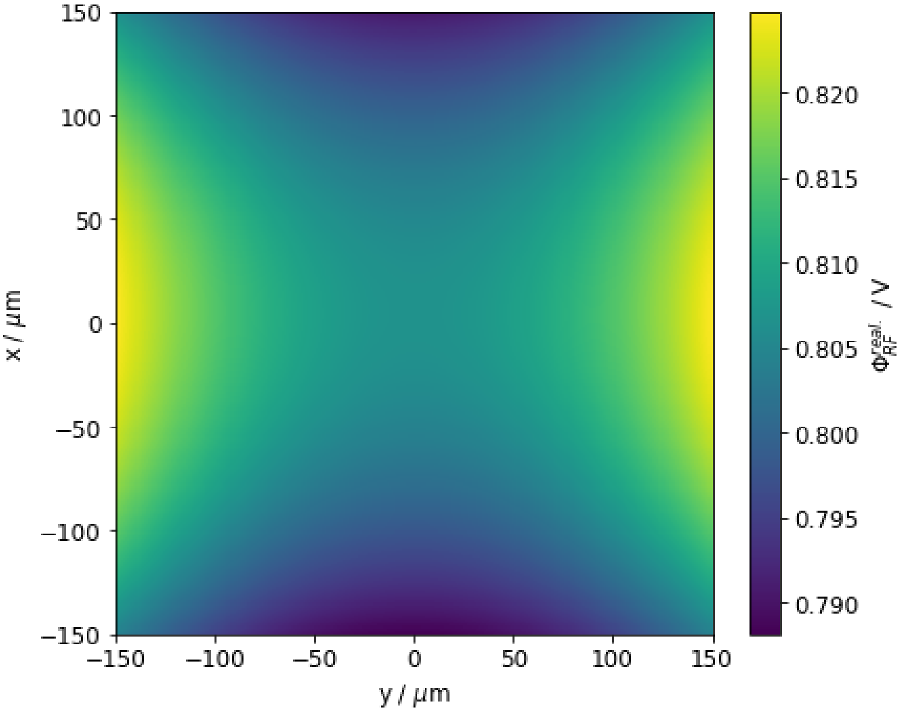

Figure 3.1.: Cross section of the RF-electrodes raw potential data at $z = 0$.

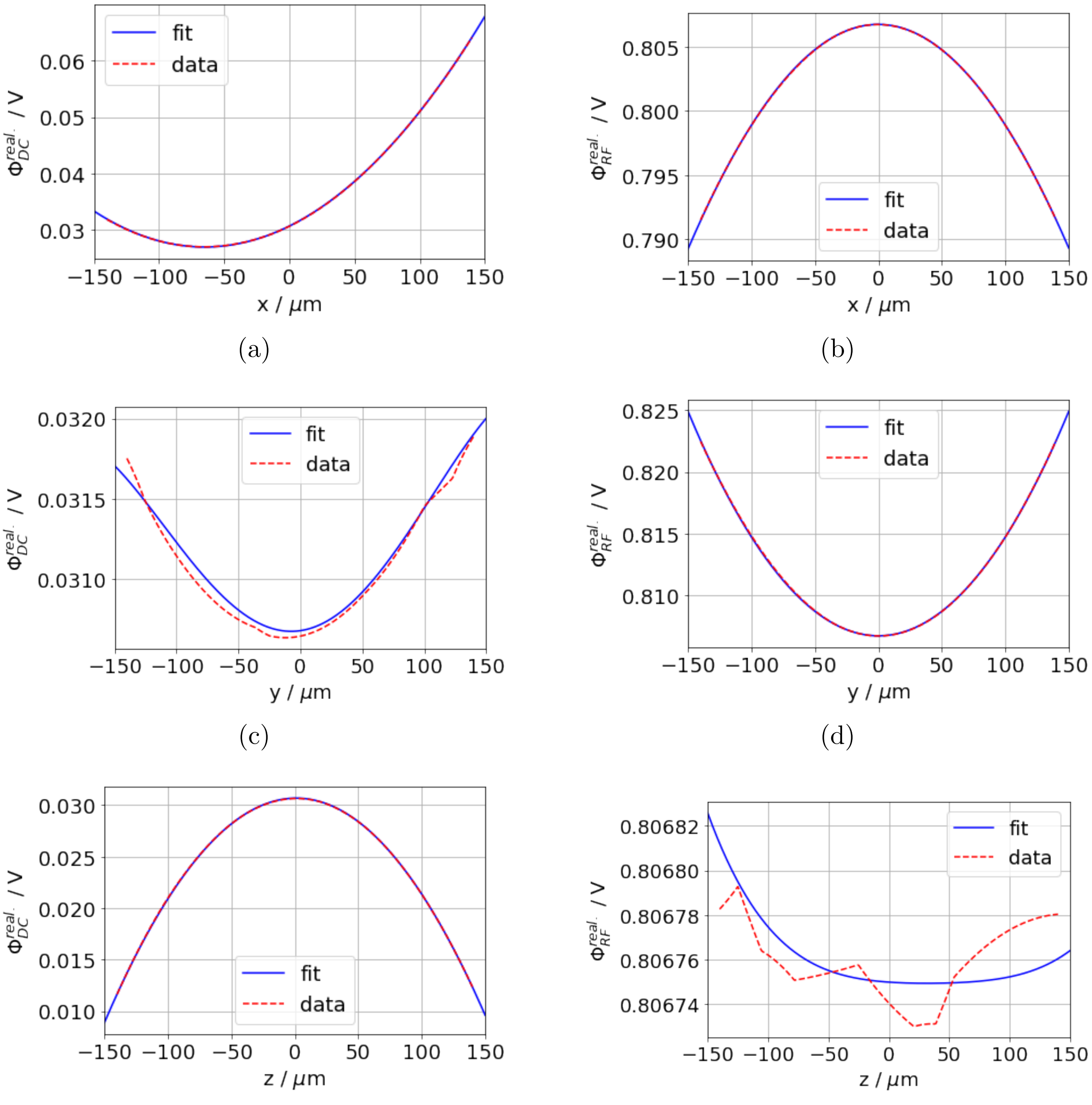

(a) (b)

(c) (d)

(e) (f)

Figure 3.2.: DC- and RF- potential data and fit to spherical harmonics expansion on x-axis: a) and b), y-axis: c) and d), z-axis: e) and f).

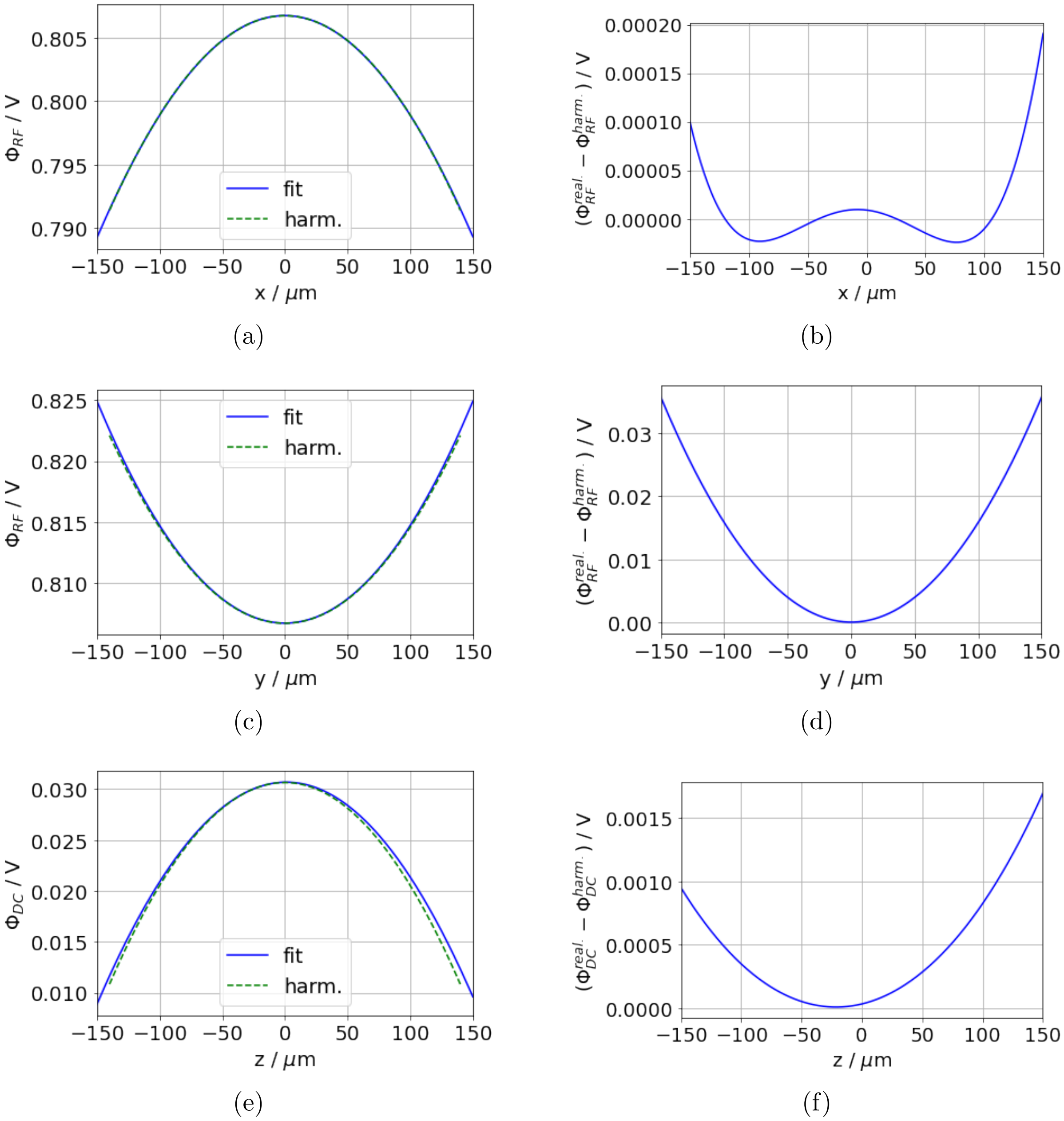

Figure 3.3.: Realistic trap potential in comparison to the purely harmonic potential (determined in section 4.1.1) in a) x-, c) y- and e) z-direction. Also, the differences of the realistic and harmonic potential $\Phi^{real.} - \Phi^{harm.}$ are shown for each component in b), d) and f).

The voltages actually applied in the experiment are roughly $U_{DC} = 0.1$ V and $V_{RF} = 90$ V (the voltages will be adjusted to give the desired motional frequencies). For the simulation, the coefficients $M_{j,DC}$ and $M_{j,RF}$ are scaled accordingly. For a trapped electron, the DC-potential is confining in axial direction and slightly repelling in radial directions. This does not disturb the trapping, because the radial DC-repulsion is overcome by a strong confining RF-saddle potential. The axial component of the RF-potential has almost no impact, being smaller than the radial components by more than two orders of magnitude. This explains also, why the fit to the spherical harmonics expansion is less accurate for this component.

A harmonic potential of the form 2.6 is used as reference in this work. The parameters U, V, etc., are determined in section 4.1.1, such that the harmonic potential provides the same motional frequencies as the realistic trap. This allows a reasonable comparison. Figure 3.3 shows the comparison of the fitted RF-potential components in radial directions and the DC-potential component in axial direction. Also shown is the difference of the realistic and the harmonic potential $\Phi^{real.} - \Phi^{harm.}$ for each component. The deviation from the harmonic potential is rather small. Overall, the realistic potential is slightly stronger in y direction and slightly weaker in x- and z direction. The differences are increasing for larger distances from the trap center. Due to the very small differences, very similar results for simulations with the realistic and harmonic potential can be expected. If at all, the anharmonicities of the realistic trap should only affect electrons with very high kinetic energies that travel far out, probing the outer potential regions.

3.2. Velocity Verlet Integration

The particle simulations in this thesis use the Velocity Verlet algorithm:

$$\mathbf{r}(t+dt) = \mathbf{r}(t) + \mathbf{v}(t)dt + \frac{1}{2}\mathbf{a}(t)dt^2, \tag{3.3}$$

$$\mathbf{v}(t+dt) = \mathbf{v}(t) + \frac{\mathbf{a}(t) + \mathbf{a}(t+dt)}{2}dt, \tag{3.4}$$

with velocity $\mathbf{v} = \dot{\mathbf{r}}$ and acceleration $\mathbf{a} = \ddot{\mathbf{r}}$. The force acting on the electron with mass m_e is calculated via the potential gradient as $\mathbf{F} = m_e\mathbf{a} = e\mathbf{E} = -e\nabla\Phi$ with the electric field $\mathbf{E}$. The algorithm integrates the corresponding equation of motion. This integration scheme is symplectic, meaning that for sufficiently small time steps it has no energy drift. Even though the numerical energy is not strictly conserved, it oscillates around the exact energy and remains bounded. This property is called quasi energy conservation and is very crucial for long term simulations of physical dynamics.

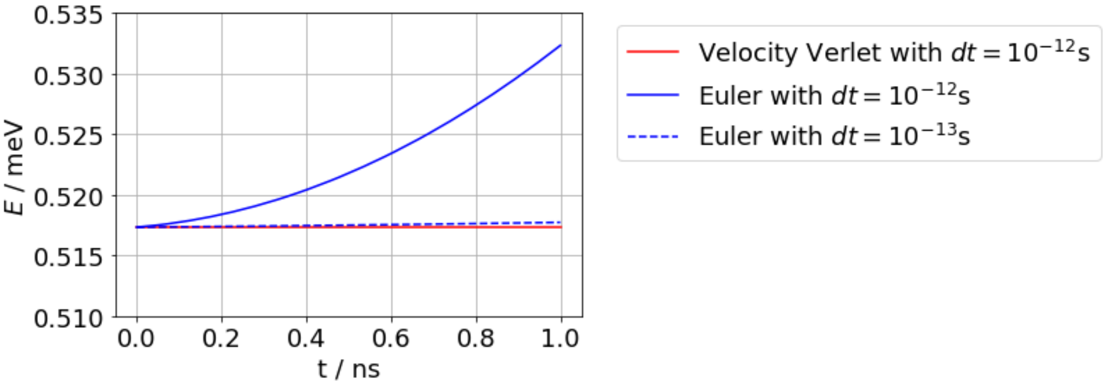

Figure 3.4.: Comparison of Velocity Verlet (red) - and Euler integration (blue), showing the total energy. In contrast to the Euler method, the Velocity Verlet integration shows no energy drift. The energy drift of the Euler method can be reduced by lowering the time step size (dashed line).

Figure 3.4 shows a comparison of a Velocity Verlet- and an Euler integration of an electron moving in a purely harmonic potential without micro motion. The electron's numerical total energy in the figure remains on a constant level for the Velocity Verlet integration with time step $dt = 10^{-12}$ s. The Euler method with the same time step size shows a strong energy drift. This energy drift can be lowered by choosing a smaller time step, increasing the computational cost. As shown by the dashed line, a decrease of the time step by more than one order of magnitude would be necessary to get similar energy conservation as the Velocity Verlet algorithm.

4. Results

The basic research question of this thesis, i.e. the **numerical investigation of the dynamics and stability of electrons in a Paul trap** by particle simulations, can now be studied, since all the necessary elements were introduced: basic physics and numerical tools for the specific system. Results for an approximated, purely harmonic potential of the shape 2.6 with the same motional frequencies are used for reference. This allows a validation of the simulations and makes it possible to determine the impact of the anharmonicities in the realistic trap potential. After a first section presenting the motional frequencies, the implementation and effects of a resistive cooling model are discussed. The coupling strength between axial and radial motional modes is investigated, i.e. how much energy is transferred between the motional modes. The result is of practical importance, because a strong coupling would imply that cooling of the axial motion would also cool the radial modes. The same would hold for heating. Finally, the formation and stability of two electron structures, i.e. the simplest version of Coulomb crystals, is discussed.

4.1. Motional Frequencies

As a first step the electron's motion of a single electron without Coulomb interaction at cryogenic temperatures of $T = 4$ K is investigated. The electron is initialised in the trap center with a kinetic energy corresponding to the most probable energy at this temperature, i.e. $E_{kin} = \frac{3}{2}k_B T$, equally distributed on the three directions. The Velocity Verlet integration is carried out with time step $dt = 10^{-12}$ s for a total time of $t_{sim} = 1$ μs. This is done for the realistic potential as well as for the harmonic potential. The trajectories of the electron are discussed to determine how far it travels away from the trap center. In both cases, the potential strength is scaled to match with the experimentally demonstrated motional frequencies of $\omega_{rad} = 2\pi \cdot 300$ MHz and $\omega_{ax} = 2\pi \cdot 30$ MHz.

The motional frequencies are determined by performing a Fourier transform of the position values over the full simulation time. Then, a Lorentzian function is fitted to the peaks of the Fourier transformation to give an accurate frequency.

4.1.1. Harmonic Potential

Equations 2.18 and 2.19 can be used to select a set of parameters ($z_0 = 3146$ μm, $r_0 = 1087$ μm, $U = 0.1$ V, $V = 90$ V) that results in motional frequencies ω_{rad} and ω_{ax} as pre-defined. Using these parameters, the axial motional frequency agreed perfectly with the prediction from 2.18, but the radial motional frequency showed some discrepancy. This can be expected since 2.19 is just approximate. The RF-potential strength was fine tuned, setting $r_0 = 1130$ μm. This potential produces the following motional frequencies: $\omega_x = \omega_y = 2\pi \cdot 294$ MHz and $\omega_z = 2\pi \cdot 30$ MHz. Figure 4.1 shows the electron's position in x, y, z direction within the first 0.05 μs, as well as the Fourier transform $\mathcal{F}$ of each component as a function of frequency. This reveals the motional frequencies in each direction. It is observed that the axial motion follows a harmonic oscillation and the radial motion is additionally influenced by the quick driving frequency. It can be concluded that the maximal amplitudes of the electron in radial and axial direction at $T = 4$ K are $\max(r_x, r_y) \approx 8$ μm and $\max(r_z) \approx 4.5$ μm, implying that the electron stays close to the central region. The electron has a slightly larger maximal amplitude in y direction than in x direction, which is due to the initial phase of the RF-field. Since the x- and y components of the RF-potential have different signs (see equation 2.6), energy is added to one of the components and removed from the other, depending on the phase of the cosine. Figure 4.2 shows a wider range of the Fourier transform of the x- and y position, such that the first sideband frequencies are visible, located at the driving frequency plus and minus the secular frequency $\Omega \pm \omega_{sec}$.

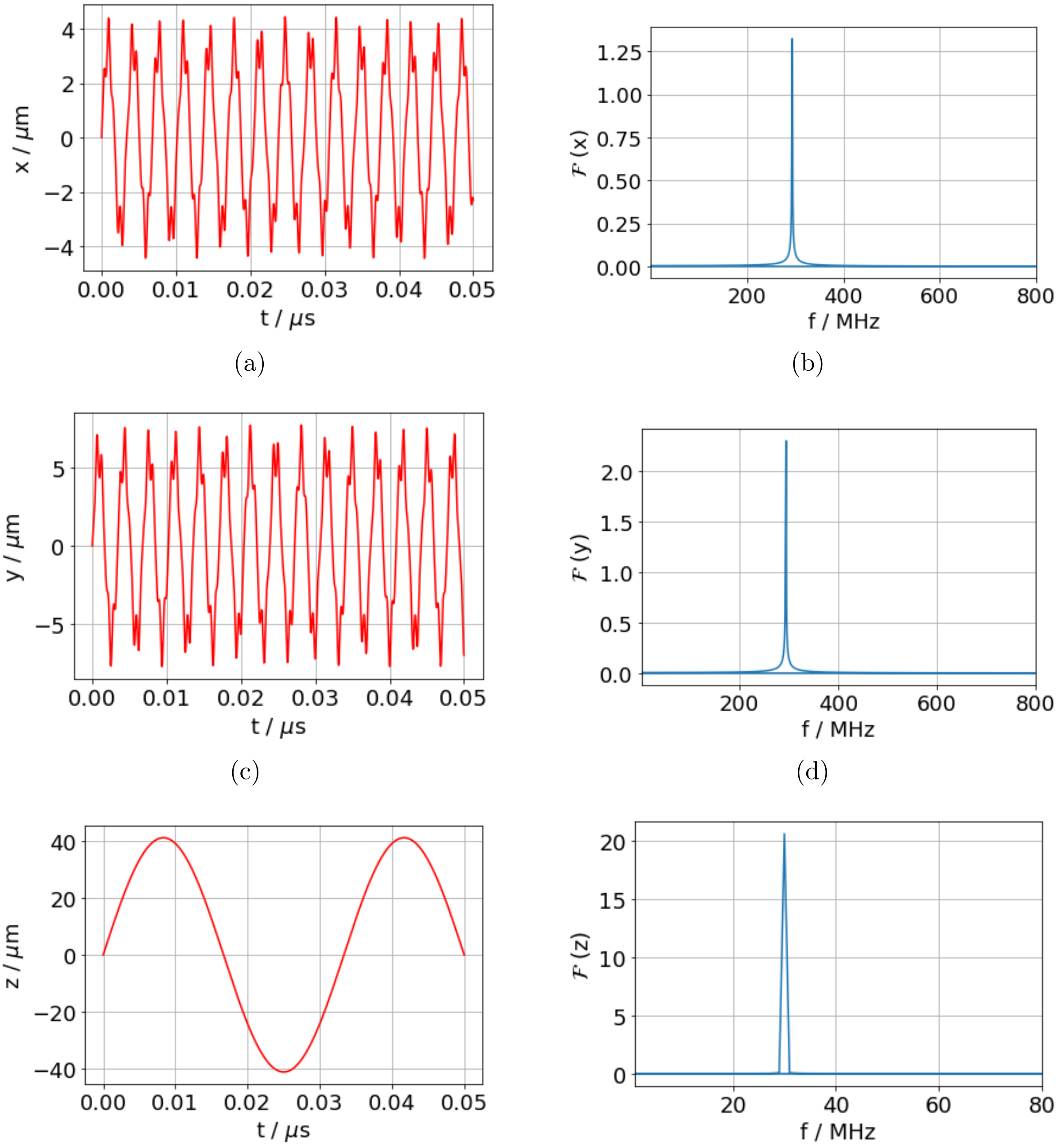

(a) (b)

(c) (d)

(e) (f)

Figure 4.1.: The position of the electron as a function of time and the Fourier transform of the position as a function of frequency for the harmonic potential in a) and b) x direction, c) and d) y direction, e) and f) z direction.

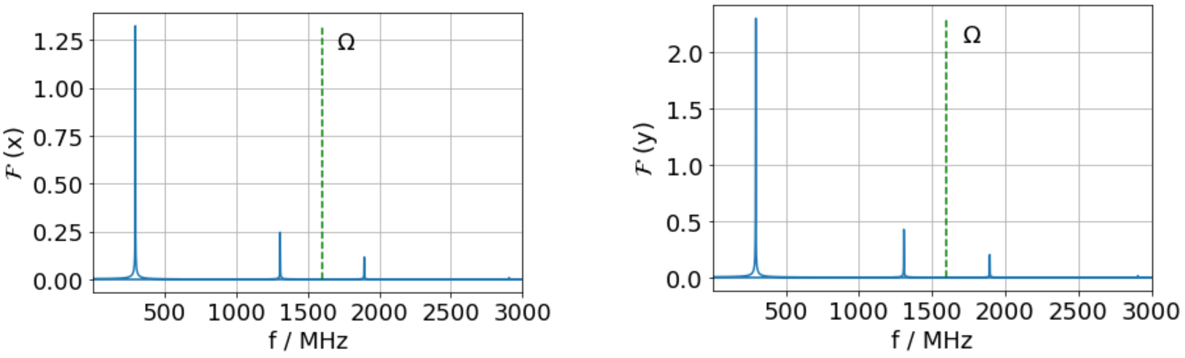

(a) (b)

Figure 4.2.: Fourier transform of the position as a function of the frequency in a) x- and b) y direction for the harmonic potential, showing the secular frequency ω_{sec} as well as the first sideband frequencies at $\Omega \pm \omega_{sec}$.

4.1.2. Realistic Trap Potential

For the realistic experimental trap potential, the voltages that have to be applied to the DC- and RF-electrodes were determined to be $U_{DC} = 0.1$ V and $V_{RF} = 90$ V. As described in the last chapter, the fitted potential expansion coefficients are scaled with these voltages to give the correct potential strength. The resulting exact motional frequencies are $\omega_x = 2\pi \cdot 295$ MHz, $\omega_y = 2\pi \cdot 296$ MHz and $\omega_z = 2\pi \cdot 29$ MHz. In contrast to the purely harmonic potential, the motional frequencies in x- and y direction differ by ≈ 1 MHz. This shows that the potential has a slightly different strength in x- and y direction due to anharmonicities. Figure 4.3 shows the position in x, y, z direction within the first 0.05 μs, as well as the Fourier transform $\mathcal{F}$ of each component as a function of frequency, giving the motional frequencies. The mean electron position is not exactly located at the trap center $x, y, z = 0$, but is slightly shifted, especially in x direction. $\langle r_x \rangle = 0.574$ μm, $\langle r_y \rangle = 0.04$ μm and $\langle r_z \rangle = 1.46$ μm are the coordinates of the traps potential minimum. To control the initial kinetic energy of the electron, the real potential minimum must be known. Initialising the electron at $x, y, z = 0$ would add potential energy to the system. The maximal deflection of the electron's motion from the potential minimum in x, y, z is similar as in the approximated harmonic potential. Figure 4.2 shows the Fourier transform of the x- and y positions as a function of frequency in a wider range, with the first sideband frequencies visible. In comparison to the harmonic potential, the Fourier transform of the electron's position shows more contributions from different frequencies, besides the main secular frequency. They originate from the anharmonicities that contribute to the potential.

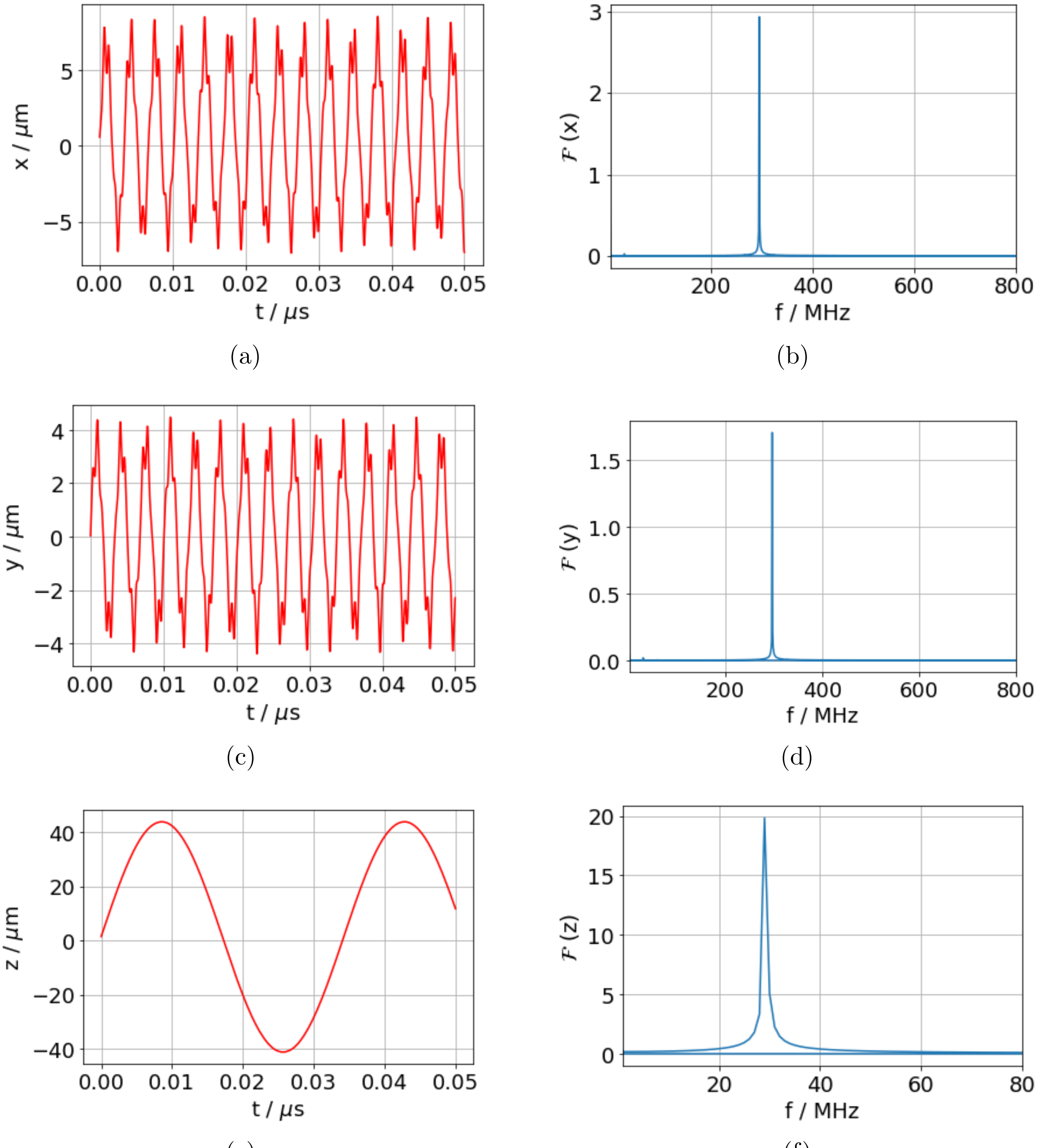

(a) (b)

(c) (d)

(e) (f)

Figure 4.3.: The electron's position as a function of time and Fourier transform of the position as a function of frequency for the realistic trap potential in a) and b) x direction, c) and d) y direction, e) and f) z direction.

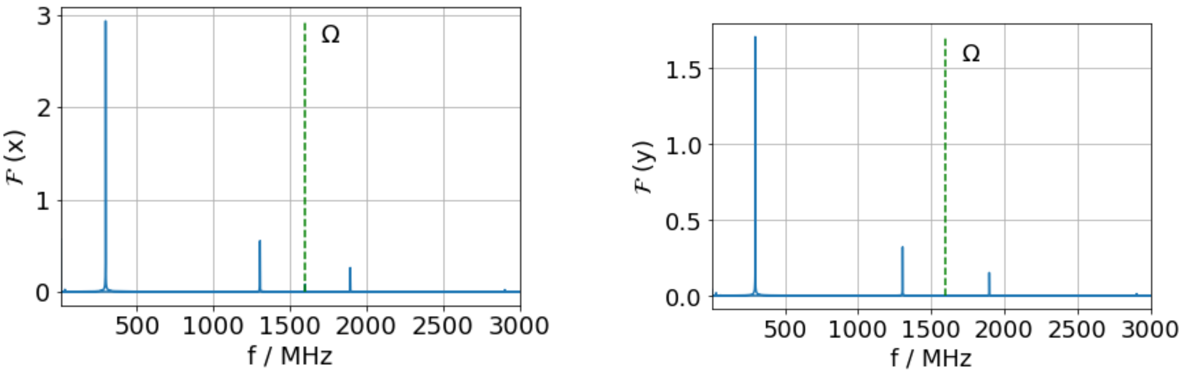

(a) (b)

Figure 4.4.: Fourier transform of the electron's position in a) x- and b) y direction for the realistic trap potential, showing the secular frequency ω_{sec} as well as the first sideband frequencies at $\Omega \pm \omega_{sec}$.

The trapping stability of the trap's potential can be tested in the simulation by varying the initial energy. In the simulation, electrons of energies up to 220 meV (equally distributed in x, y, z) are trapped reliably. This matches well with the stability found in some first experiments on this trap, as verified in personal communication with the Trapped Ions group.

4.2. Axial Cooling and Johnson Nyquist Noise

The ability to cool the trapped electrons is crucial for their feasibility as qubits. This is realised via resistive cooling, using a tank circuit that is coupled to the electron's motion, as described in section 2.4. In this work only a single cooling tank circuit, applied in axial direction, is assumed. This was the originally proposed experimental setup in [1]. The resistive cooling itself can be implemented easily within the numerical integration by adding a velocity dependent damping force to the equation of motion as described by equation 2.38. The Johnson Nyquist noise that comes along with this cooling method is modelled as follows: an additional random force is generated during every integration time step, following a Gaussian distribution, and applied during the current time step. This means that a constant noise force is acting on the system for a duration of the time step length dt. The Gaussian distribution of the noise has the mean $\langle U_{noise} \rangle = 0$ and the variance $\langle U_{noise}^2 \rangle = 4 k_B T_{res} R \Delta f$.

The Johnson Nyquist noise model desribed before is applied in a simulation of a purely harmonic potential with motional frequencies $\omega_{ax} = 2\pi \cdot 50$ MHz and $\omega_{rad} = 2\pi \cdot 450$ MHz. Further parameters used for the test case are the resistance $R = 500$ kΩ, resistor temperature $T_{res} = 0.4$ K and effective distance $d_{eff} = 300$ μm, all in accordance with former and prospective trapped electron experiment as discussed in [1]. Since the bandwidth Δf of Johnson Nyquist noise in a resistor is not known, it is treated as a free parameter. Initialised with temperature $T_{ax} = T_{rad} = 4$ K and corresponding thermal kinetic energy, a single trapped electron is tracked with cooling and noise contributions over a time period of 50 μs. The resulting axial equilibrium temperature is determined by averaging the kinetic energy in axial direction as described by 2.40. In this energy average, the first 10 μs are neglected, since the active cooling period of the system can be assumed completed after this time period. This can be determined by diagnosing the energy change over time.

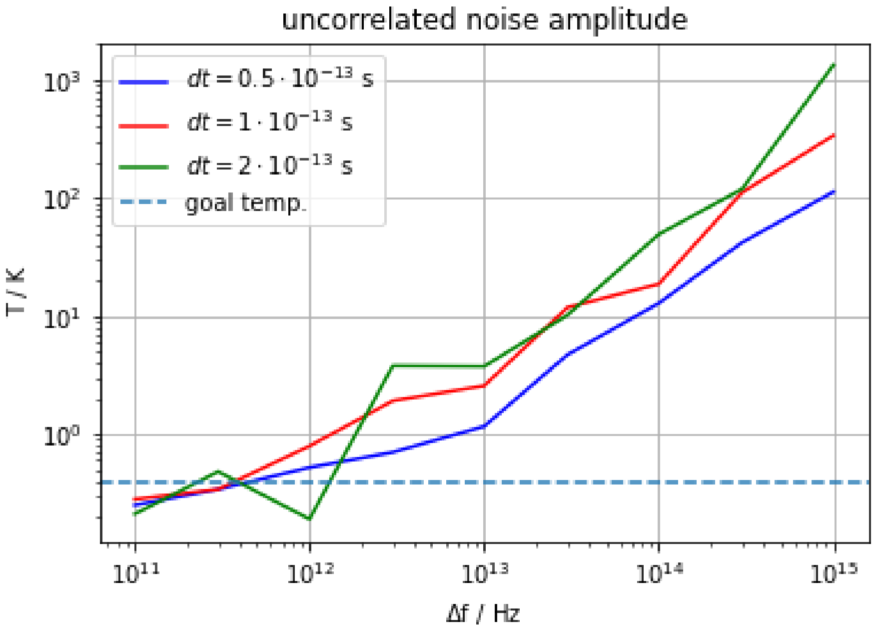

Figure 4.5.: Axial equilibrium temperature $T_{eq,ax}$ as a function of the bandwidth Δf for three different time steps sizes. The target temperature is marked by the dashed horizontal line.

Figure 4.5 shows the resulting axial equilibrium temperature $T_{eq,ax}$ as a function of the bandwidth for three different time step lengths $dt = 0.5 \cdot 10^{-13}$ s (blue), $dt = 1 \cdot 10^{-13}$ s (red) and $dt = 2 \cdot 10^{-13}$ s (green). A larger bandwidth is equivalent to a larger noise amplitude, resulting, as expected, in a higher kinetic energy and equilibrium temperature. Another observation is that, besides the noise strength, the equilibrium temperature depends also on the chosen time step length. Longer time steps result in slightly higher temperatures than shorter time steps. This can be explained as follows: a longer time step means that the randomly distributed noise force, generated during every time step, acts on the electron for a longer time and thus drags it further away from the average motion, adding more energy to the system. However, it is not at all desirable to include an artificial time step dependency for the model approach, because this is an artifact of the integration method. To get rid of this, the bandwidth is set to be proportional to the inverse time step with a bandwidth scaling constant C_{bw}, such that $\Delta f = \frac{C_{bw}}{dt}$. The proportionality to the inverse time step is reasonable, since frequencies much smaller than $\frac{1}{dt}$ do not have enough time to contribute significantly to the noise, while contributions of frequencies that are much larger will average out.

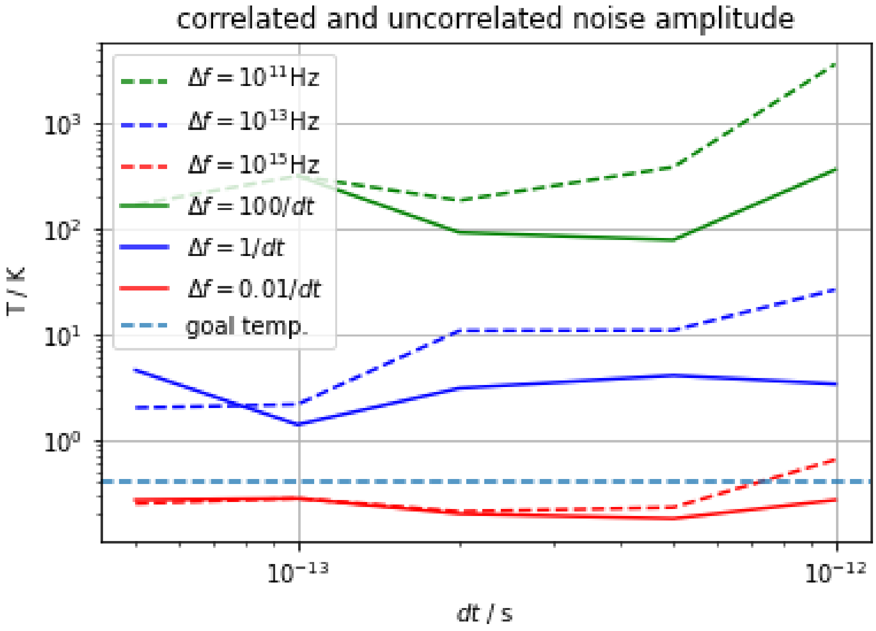

Figure 4.6.: Axial equilibrium temperature $T_{eq,ax}$ as a function of the time step dt. If the noise amplitude is independent from the time step, the temperature rises slightly with larger time steps (dashed curves). For a noise amplitude that is correlated with the time step, the dependency of the temperature on the time step can be eliminated (solid curves). The target temperature is marked by the dashed horizontal line.

Figure 4.6 shows a comparison of the equilibrium temperature $T_{eq,ax}$ as a function of the time step dt for uncorrelated noise amplitudes for three different fixed bandwidths (dashed lines). The equilibrium temperature for correlated noise amplitudes that are dependent on the time step dt and scaled with three different scaling factors C_{bw} (continuous lines) are also plotted. For the uncorrelated noise amplitudes with constant bandwidth, the temperature increases slightly for longer time steps as shown before in figure 4.5. If the bandwidth is correlated with the time step, the temperature stays on a constant level for increased time steps. This means that the dependency of the temperature on the time step can be avoided using this model for Δf. The final temperature is then only dependent on the scaling factor C_{bw}.

In the following, the resistive cooling model introduced before is implemented for simulations of the particular electron trap investigated in this thesis with motional frequencies of $\omega_{ax} = 30$ MHz and $\omega_{rad} = 300$ MHz. All physical parameters are chosen according to parameters of current and future trapped electron experiments. The trap is kept at a cryogenic temperature $T = 4$ K, which defines a corresponding initial energy of the trapped electron in both radial and axial directions. Separately, the tank circuit for readout and cooling with resistance $R = 5$ MΩ is kept at a lower temperature of $T_{res} = 0.4$ K. The resistance was chosen larger than in the experiments to reduce the cooling time and thus the computation time. The effective distance between the pick-up electrodes can be estimated within the Ansys software as $d_{eff} = 1$ mm. It should be mentioned that the model discussed here neglects all other sources of noise that exist in an experimental setup, besides the Johnson Nyquist noise of the tank circuit's resistor. A detailed overview of the impact of different sources of electric field noise is provided in [16]. However, in the setup discussed in this thesis the Johnson Nyquist noise of the tank circuit can be assumed to dominate. This is achieved by the design, as the tank circuit used for resistive cooling is chosen to match the electron's resonance frequency. Another simplification assumed here is the modeling of the tank circuit itself as a plate capacitor with the electron in between. This is not an exact representation of the physical system. The electrodes do not provide a perfectly homogeneous electric field. Nevertheless, this approach is reasonable for cold electrons near the trap center. The problem of noise in Paul traps for electrons is a rather complex problem, with a large potential for further research.

The scaling factor C_{bw} is treated as a free parameter. The equilibrium temperature in the axial direction is equal to the temperature of the resistor $T_{eq,ax} = T_{res}$ as known from former experiments and described in section 2.4. By varying the scaling factor of the bandwidth C_{bw} and thus the noise strength and monitoring the resulting equilibrium state, it is possible to determine the correct value for C_{bw}. This is done in the following for both the realistic trap potential as well as for the purely harmonic potential, simulating a single electron.

The results of the bandwidth variations are shown in figure 4.7. They were found by averaging the axial kinetic energy after the cool-down phase over a time period of 60 μs. The longer the averaging time period, the more accurate is the resulting value of the equilibrium temperature. Close to the matching factor which results in equilibrium temperatures close to the target temperature of 0.4 K, the simulation was carried out repeatedly for four times and the temperature average was taken. The best matching bandwidth scaling factor is found to be $C_{bw} = 0.16$, implying a bandwidth of $\Delta f = 1.6 \cdot 10^{12}$ Hz, for the realistic trap potential as well as for the harmonic potential. With this value for the bandwidth scaling factor, the average resulting equilibrium temperature is $T_{eq}^{harm.} = 0.37$ K for the harmonic potential and $T_{eq}^{real.} = 0.39$ K for the realistic potential. This is sufficiently close to the desired 0.4 K. A verification of the determined noise strength is only possible by measuring the noise power experimentally. This should be done in future related trapped electron experiments.

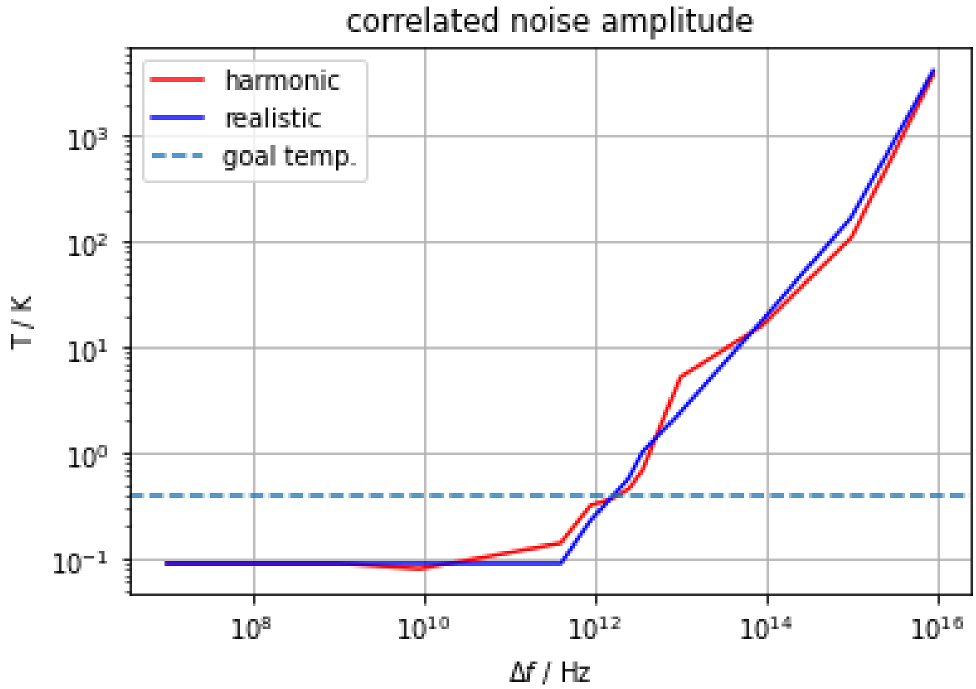

Figure 4.7.: Axial equilibrium temperature for the harmonic potential (red) and realistic potential (blue) as a function of the Johnson Nyquist noise bandwidth Δf, i.e. the noise strength. The target temperature of 0.4 K is marked by the dashed line.

The correct noise strength for modelling the experimental system has now been determined and further investigations can be started. Since the system is following a stochastic process, simulation results will differ in detail, but follow similar dynamics. Figure 4.8 shows examples of the electron's kinetic energy in axial direction as a function of time in the realistic potential as well as in the harmonic potential. Within about the first 20 μs the motional energy is damped with fluctuations from its initial value to the 0.4 K level. The electron's energy is following a $1D$ Boltzmann distribution, as shown in figure 4.9. This observation is a good evidence for the quality of the noise model used for the simulations, as it matches not only the theoretical expectations but also the experimental findings described in 2.4.

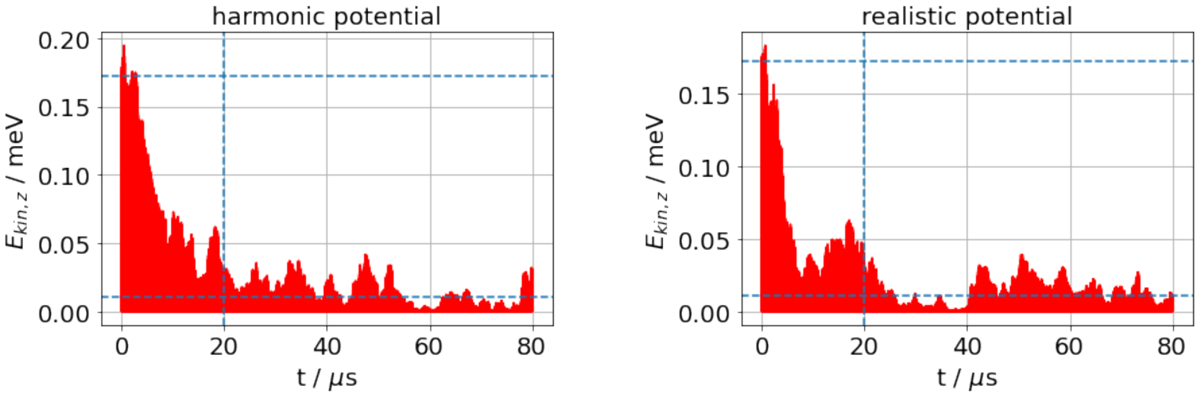

(a) (b)

Figure 4.8.: Axial kinetic energy for a) the harmonic potential and b) the realistic potential, with resistive cooling and Johnson Nyquist noise modelling. The dashed horizontal lines mark the initial (upper line) and target mean energy (lower line). The vertical dashed line marks the beginning of the energy averaging time period that was used to calculate the resulting axial equilibrium temperature.

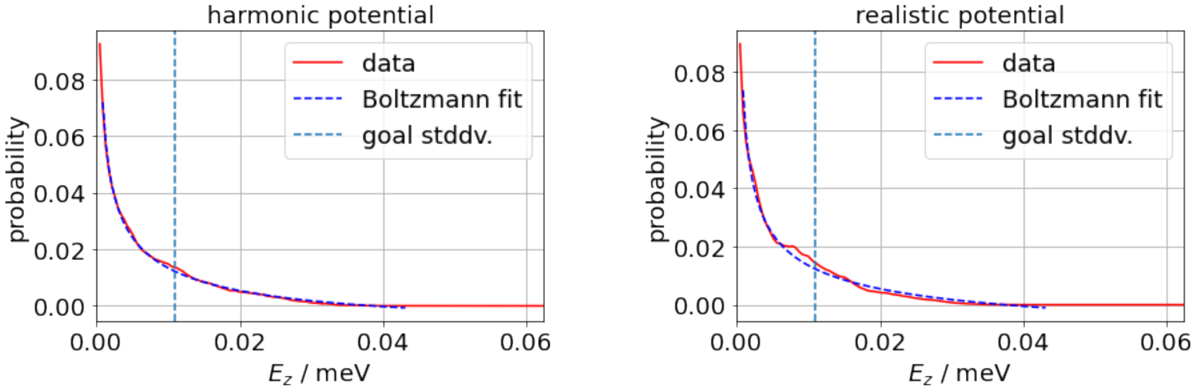

(a) (b)

Figure 4.9.: Axial kinetic energy distribution for a) the harmonic potential and b) the realistic potential, with resistive cooling and Johnson Nyquist noise modelling. The distribution is calculated after the cool-down phase of 20 μs (red curve). Also shown is the fit to a $1D$ Boltzmann distribution (dashed curve) and the target standard deviation of the distribution (dashed vertical line).

The damping constant of the tank circuit can be extracted from the energy auto-correlation function $c_{EE}(t, t+\tau)$ as discussed in section 2.4. The auto-correlation function is decreasing exponentially with τ_{decay} as shown in figure 4.10. The decay time constant τ_{decay} is equal to the tank circuit's damping constant. It is in the range of 3 - 8 μs for various simulation runs. The average over 4 simulations is $\tau_{decay}^{harm.} = 5.3$ μs for the harmonic potential and $\tau_{decay}^{real.} = 5.8$ μs for the realistic potential. The tank circuit cools the electron's motion in the realistic trap potential equally efficient as in the harmonic potential. The slight difference between the cooling times is within statistical variations.

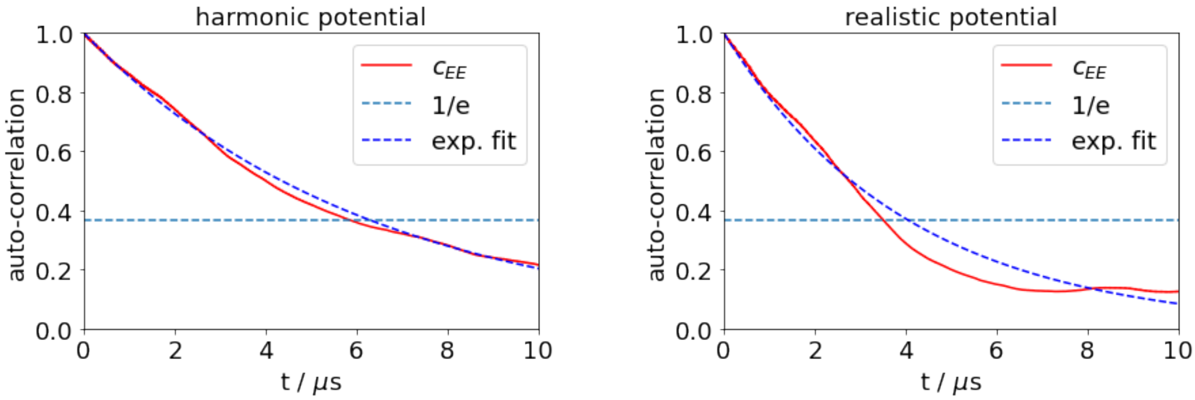

(a)

(b)

Figure 4.10.: Auto-correlation function of the axial energy for a) the harmonic potential and b) the realistic potential, showing an exponential decay. The dashed horizontal line marks the 1/e decay level that is reached after a couple of μs. The dashed curve shows the fit to an exponential decay function.

Calculating the theoretical estimate of the tank circuit's cooling time constant via

$$\tau_{decay} = \frac{m_e d_{eff}^2}{e^2 R} \tag{4.1}$$

for the circuit's values of d_{eff} and R gives the same order of magnitude: $\tau_{decay} = 7$ μs. It matches quite well with the cooling constants observed in the simulated systems.

A discrepancy of a couple of μs is consistent with statistical errors. Future work on the simulation could determine a more accurate value of the cooling time constant by averaging over more than just four simulations. Also, the average equilibrium temperature for the used noise strength lies slightly below 0.4 K. This might explain why the average damping constant lies also slightly below the theoretical expectation.

4.3. Coupling Strength between Axial and Radial Motion

To understand the dynamics of a two electron system it is important to investigate the coupling of different motional modes. This is done in the following chapter for different physical scenarios, using the realistic trap potential. The main question is the energy transfer between different motional modes.

4.3.1. Without Coulomb Interaction

At first, the simplest scenario of a single trapped electron is investigated. It is initialised in the trap center with kinetic energies corresponding to $T = 4$ K. The simulation is carried out with time step $dt = 10^{-12}$ s. The kinetic energy in x, y, z direction is tracked over a time period of 80 μs and is shown in figure 4.11. The tank circuit applied in axial direction causes a reduction of the kinetic energy in z direction, as discussed in the previous section. In the observed period of time, the tank circuit has no impact on the radial energy. The kinetic energy in radial direction remains on a constant level. It can be concluded that without Coulomb interaction of multiple trapped electrons, the anharmonicities in the realistic trap potential do not induce an energy transfer between radial and axial modes. This also implies that it is not possible to reduce the radial motional energy using an axial cooling circuit. Additional cooling circuits in radial direction are needed and can be implemented in the experiment, as stated by Prof. Häffner during personal communication.

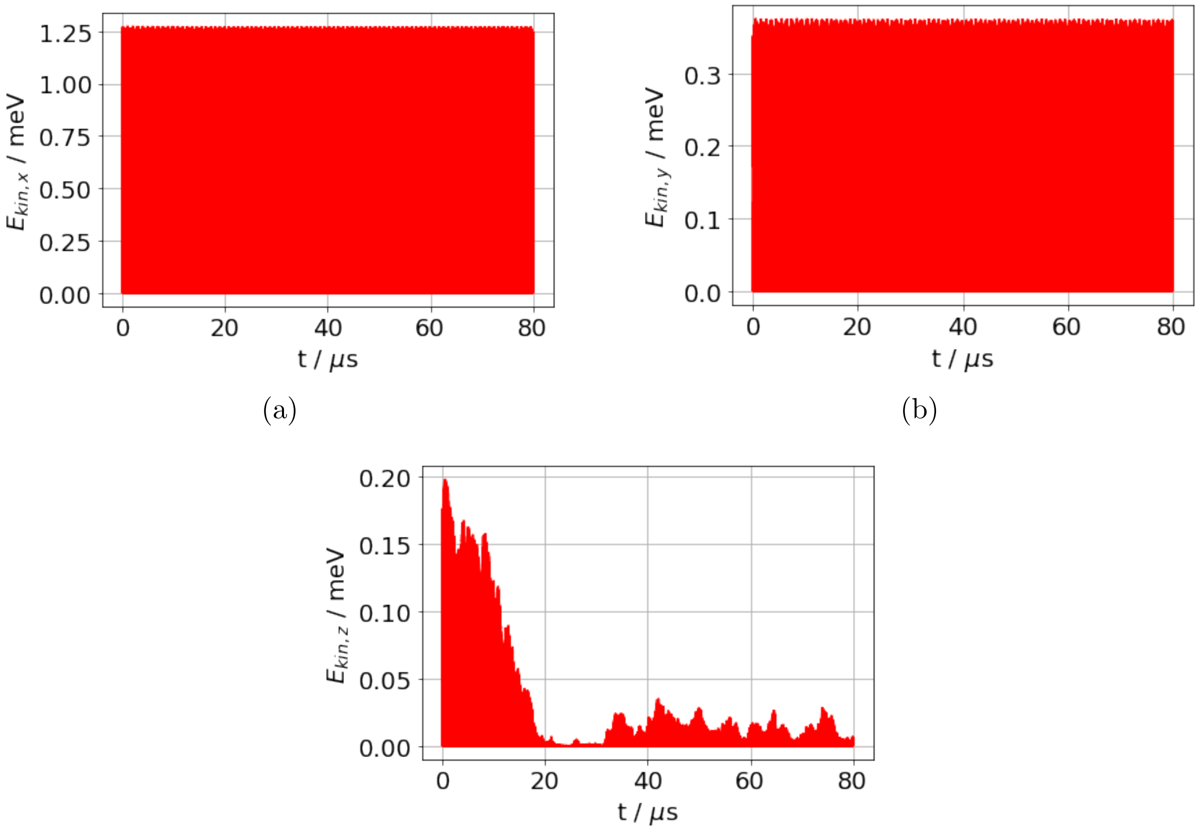

(a)

(b)

(c)

Figure 4.11.: Kinetic energy in a) x direction, b) y direction and c) z direction of a single electron in the realistic trap potential.

4.3.2. Two Electrons in Gas State

Having two electrons, trapped in the same potential, the dynamics becomes more complicated due to the Coulomb interaction. We initialise two electrons with energies corresponding to $T_{rad} = 8$ K in both radial directions and $T_{ax} = 0.4$ K in axial direction. At these energies the electrons move freely, i.e. they are in a 'gas state'. Their kinetic energy is too high to form a quasi stable Coulomb crystal. It is sufficiently high to overcome the Coulomb- and confining forces that ensure crystallisation for lower energetic electrons. Due to the Coulomb interaction, a smaller time step of $dt = 10^{-13}$ s is necessary for simulations with more than one electron. Again we have the cooling tank circuit applied in axial direction and keep track of the sum of the kinetic energies of the electrons in x, y, z direction and the sum of their total kinetic energies. The results are shown in figure 4.12. As mentioned before in section 2.3, multiple electrons in a gas state within the same trapping potential are affected by RF-heating. This heating mechanism results from Coulomb collisions between the particles in the alternating RF-field, as described in section 2.3. We can observe this mechanism in the simulation. The kinetic energy in radial and axial directions is fluctuating strongly and overall it is increasing. The axial cooling circuit does not compensate this heating mechanism. To overcome RF-heating and freeze a pair of electrons into a crystal state, additional cooling is necessary, i.e. radial cooling and potentially stretch- and zigzag mode cooling.

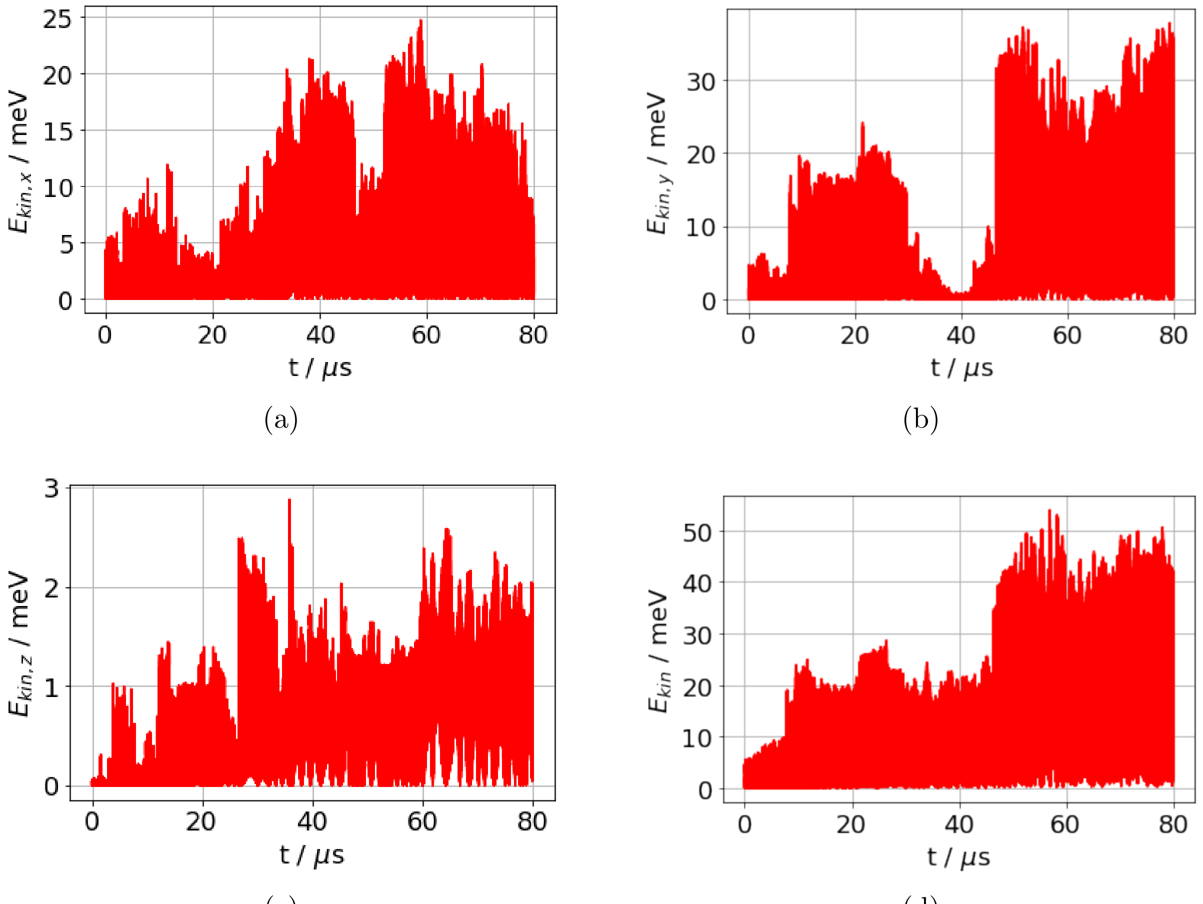

(a) (b) (c) (d)

Figure 4.12.: Kinetic energies in a) x direction, b) y direction, c) z direction and d) total kinetic energies of two trapped electrons in the gas state in the realistic trap potential.

4.3.3. Two Electrons in Crystal State

We now start with two electrons in the crystal state. This is the case for initial energies corresponding to $T_{rad} = 4$ K and $T_{ax} = 0.4$ K. These energies are low enough that the Coulomb- and confining forces keep the electrons localised at their equilibrium positions. The electrons' relative positions are monitored as explained in the following section, to ensure the crystal stability throughout the whole simulation. The initial kinetic energy is applied completely to the stretch- and zigzag modes, described in section 2.3. Now the situation is fundamentally different from the previous discussed gas state, as shown in figure 4.13. As already mentioned in section 2.3, the crystal state prevents the system from RF-heating because it suppresses strong Coulomb collisions. There is no overall heating visible in the system, which is a huge advantage. The kinetic energy remains constant in radial directions. In axial direction, the noise of the tank circuit influences the results. Also in this direction there is no heating. Within the simulated time span of 80 μs, no energy transfer from the high energy radial modes to the low energy axial mode is happening. This means that there is no strong coupling via trap anharmonicities or Coulomb interaction in the crystal state. As a consequence, just like in the single electron system, the radial modes need separate and additional damping to achieve motional cooling.

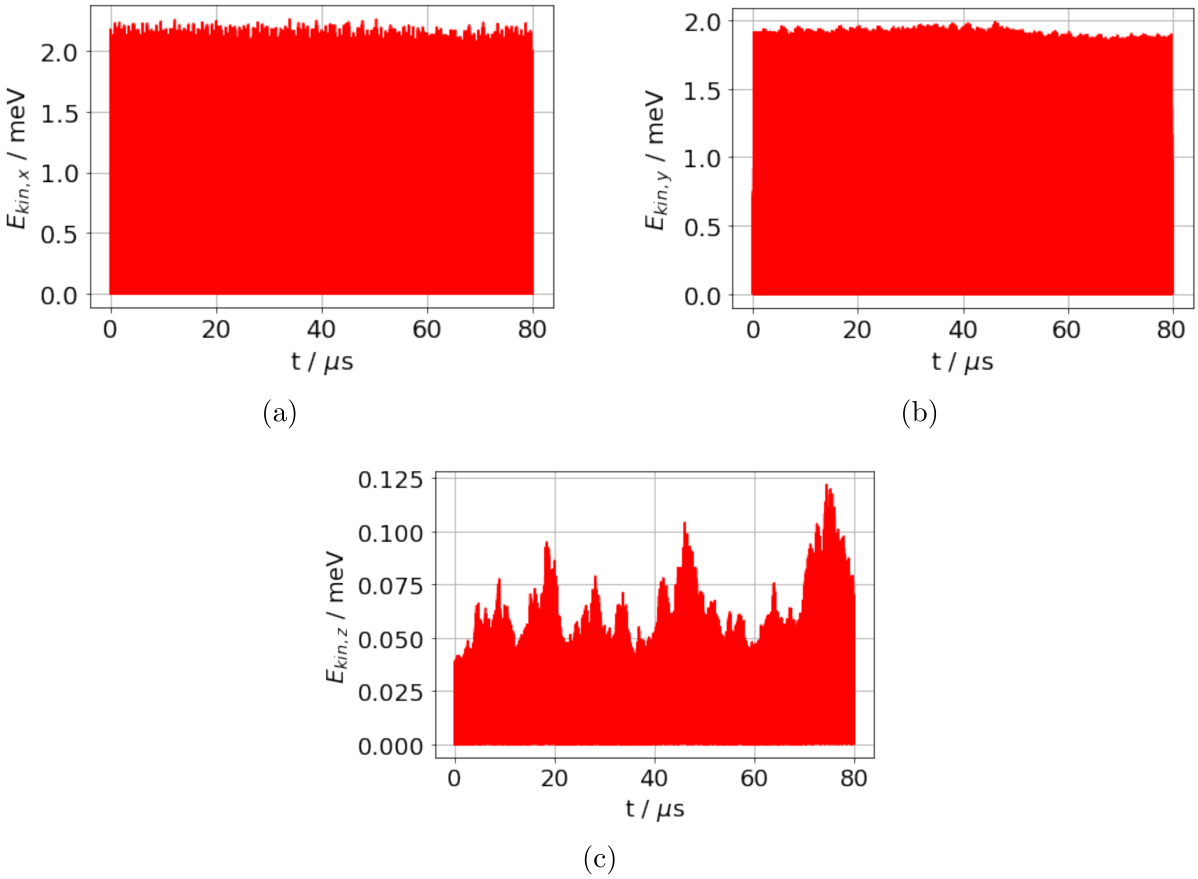

(a)

(b)

(c)

Figure 4.13.: Kinetic energies in a) x direction, b) y direction and c) z direction of two trapped electrons in the crystal state within the realistic trap potential.

4.4. Two-Electron Coulomb Crystals

In this final chapter the dynamics and stability of two-electron Coulomb crystals in the trap is investigated in detail. The numerical simulation results can provide a prediction for future experiments on trapped electron crystals. At first, the general dynamics of a two-electron system in the Paul trap is discussed. Especially interesting is the electron motion relative to the center-of-mass motion, i.e. the stretch- and zigzag modes. All simulations are carried out with time steps $dt = 10^{-13}$ s.

4.4.1. Stretch- and Zigzag Mode

We start with a very basic system to build a better understanding of the problem. Figure 4.14 shows an example of crystal dynamics in the realistic potential, without damping and noise effects. We will refer to the two electrons as electron 0 and electron 1. They are initialised at their equilibrium positions on the z-axis, 24 μm apart from each other, due to the Coulomb repulsion. Initial thermal velocities corresponding to 0.4 K are applied in axial and radial directions each, with opposite signs for electron 0 and electron 1. As a result of these initial conditions, the center-of-mass motion is zero, while the relative motion is oscillating out of phase in all three directions. In radial directions the oscillation is centered around zero, while the electrons remain separated in axial direction.

If the axial oscillation is out of phase as in this example, a strong stretching and compressing of the Coulomb crystal is observed. Therefore, this is called a stretch mode, as mentioned in section 2.3. From equations 2.34 and 2.35 we obtain: $\omega_{stretch} = 2\pi\cdot 50$ MHz, $\omega^{x}_{zigzag} = 2\pi\cdot 294$ MHz, $\omega^{y}_{zigzag} = 2\pi \cdot 295$ MHz for the realistic trap potential and $\omega^{harm.}_{stretch} = 2\pi \cdot 52$ MHz, $\omega^{harm.}_{zigzag} = 2\pi \cdot 293$ MHz for the harmonic potential. The frequencies of the stretch- and zigzag modes can be obtained by applying a Fourier transform $\mathcal{F}$ on the relative electron position $\mathbf{r}_{rel}$. This is shown in figure 4.14 for the realistic trap potential. Depicted are the relative positions of both electrons as a function of time, as well as their Fourier transform as a function of the frequency. The same simulation was done for the harmonic potential. The Fourier transform is applied over a time of 0.5 μs. We find $\omega_{stretch} = 2\pi \cdot 52$ MHz, $\omega^{x}_{zigzag} = 2\pi \cdot 292$ MHz, $\omega^{y}_{zigzag} = 2\pi \cdot 293$ MHz for the realistic trap potential and $\omega^{harm.}_{stretch} = 2\pi \cdot 53$ MHz, $\omega^{harm.}_{zigzag} = 2\pi \cdot 290$ MHz for the harmonic potential. This is in good agreement with the above predictions.

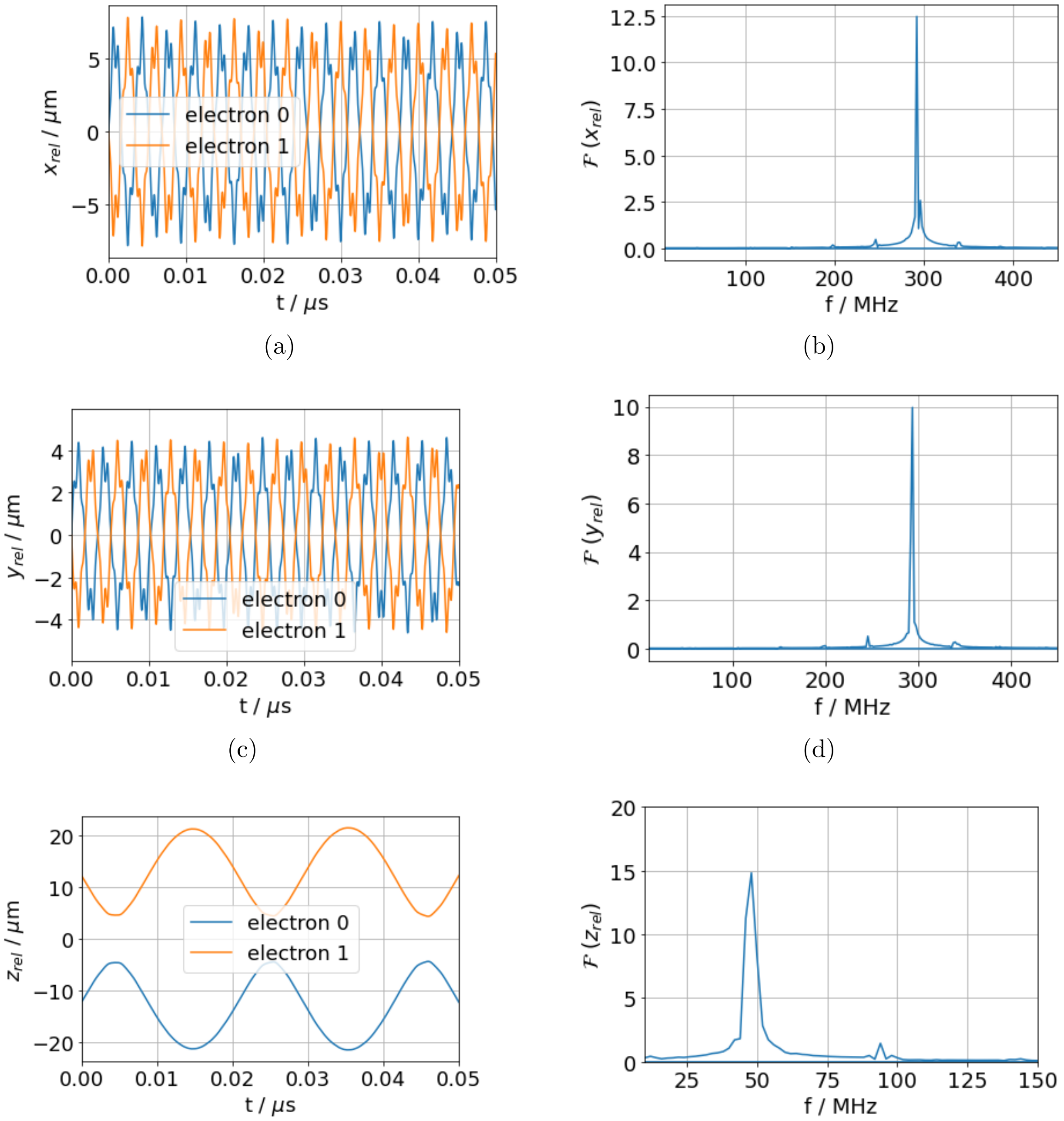

(a) (b)

(c) (d)

(e) (f)

Figure 4.14.: Dynamics of a two-electron crystal in the realistic trap potential at 0.4 K. Shown are the relative positions of both electrons as a function of time a), c), e) as well as their Fourier transform as a function of frequency b), d), f). Based on the initial conditions, the electrons are oscillating out of phase. In radial directions a) and c) the oscillation is centered around zero. In axial direction c) the electrons remain separated. The corresponding Fourier transform $\mathcal{F}$ of the relative position give the frequencies of the zigzag modes b) and c) and of the stretch mode f).

The electrons are aligned on the weakest trapping axis, i.e. the z-axis. Therefore the axial separation is dominating the total distance of the electrons as shown in figure 4.15 for $T_{ax} = 0.4$ K and $T_{rad} = 4$ K. Depicted is the distance between both electrons split into x-, y- and z components, as well as the total difference as a function of time. As a criterion of the crystal state, the signs of the relative electron positions in z are used. If the signs flip, the electrons have switched positions. If such events happen, it is no longer possible to determine which electron is located on which side. Therefore the crystal is 'broken' in terms of serving as qubits.

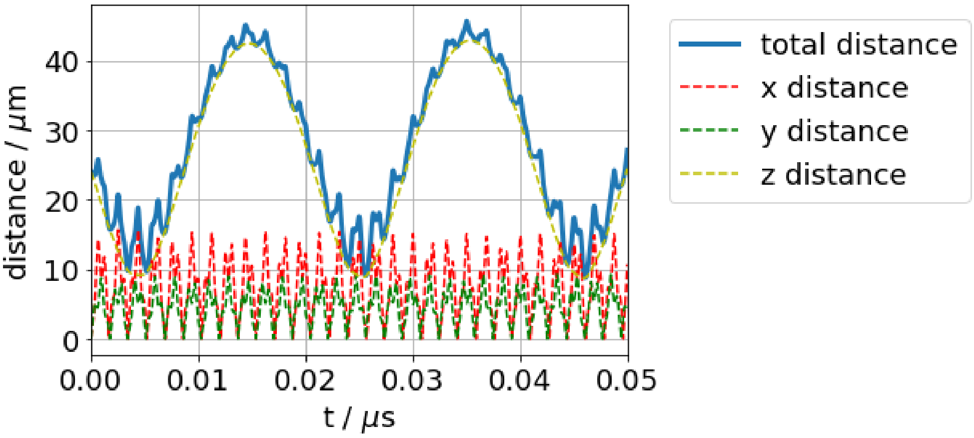

Figure 4.15.: Distance of electrons in a two-electron crystal at $T_{ax} = 0.4$K and $T_{rad} = 4$K. The total distance is mainly dominated by the distance in z, while the distance in x and y is comparably small.

Resistive cooling can only be used to reduce the kinetic energy of the center-of-mass mode. It has no direct impact on the stretch mode. Whether there is energy transferred between the stretch- and center-of-mass mode is not yet answered. It could still be a balancing effect due to Coulomb interaction and trap anharmonicities that would allow cooling of the stretch mode. A simulation is carried out on a two-electron crystal, tracking the kinetic energy of both the stretch- and center-of-mass mode. The radial zigzag modes are initialised with $T_{rad} = 0.4$ K each, the axial stretch mode with $T_{ax} = 1$ K. With these initial conditions the crystal remained stable within the time simulated. Initially, the center-of-mass motion is zero. The cooling tank circuit is applied in axial direction with $T_{res} = 0.4$ K.

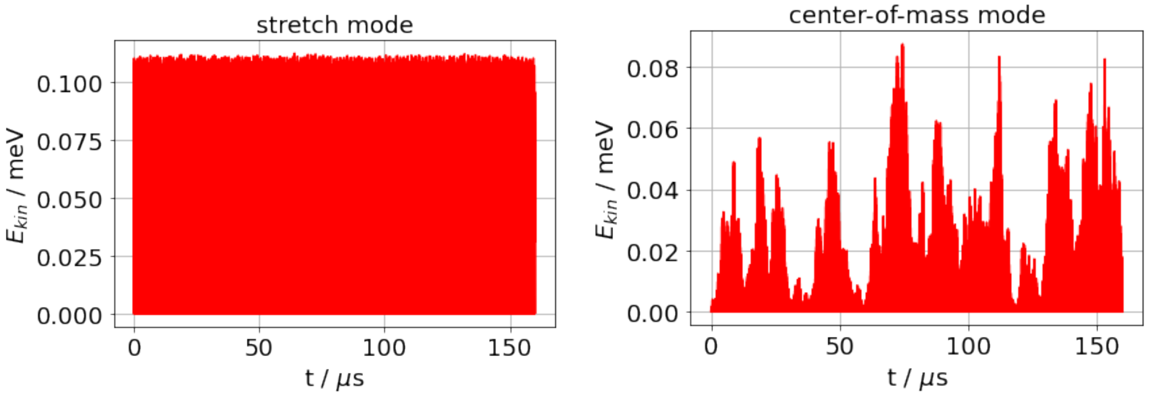

(a) (b)

Figure 4.16.: Kinetic energy in z direction as a function of time, split into a) stretch mode and b) center-of-mass mode.

Figure 4.16 shows the resulting kinetic energy in the stretch- and centre-of-mass mode over the simulated time period of 160 μs. Within this time period, there is no energy transfer from the high energy stretch mode to the low energy center-of-mass mode. The stretch mode energy remains constant while the center-of-mass energy is following the tank circuit's Johnson Nyquist noise. It is 'heated' up from the initial zero energy level to the tank circuit's 0.4 K. Cooling of the stretch mode is thus not possible with this method. The problem of cooling the stretch mode can be overcome with other strategies. One possible option is cooling the electrons separately, before merging them into a cold crystal.

4.4.2. Crystal Stability

Whether a Coulomb crystal is stable or not depends crucially on the stretch- and zigzag mode energy. High relative energies allow the electrons to switch positions, overcoming the force of the trapping potential and their own Coulomb repulsion. Therefore, this section focuses on investigating this dependency further. Simulations are carried out with two-electron crystals, initialised with kinetic energy only in the stretch- and zigzag modes and no kinetic energy in the center-of-mass modes. This scenario is equivalent to the scenario discussed in the section above. The electrons are oscillating out of phase. In addition, the tank circuit in axial direction is applied. For various initial energies it is observed, whether and after what time period the electrons switch positions, i.e. the crystal 'breaks apart' for the use as a qubit. This time span before a switching event occurs will be referred to in the following as the crystal 'lifetime'. The simulations are stopped after a time of 160 μs. Therefore, this is the maximal lifetime a crystal can reach in this study.

A first scan is carried out for different radial initial energies, i.e. zigzag mode energies. The axial energy is always initialised corresponding to $T_{ax} = 0.4$ K and, due to the tank circuit, follows a Boltzmann distribution of this temperature. Figure 4.17 shows the resulting crystal lifetimes as a function of the radial energy. For a better visualisation, the same results are shown on log scale as well. The graphs show the average lifetime over three simulations. The results for the realistic trap potential are compared to the harmonic potential. In both cases, the crystal is surviving the 160 μs simulation for radial energies below $T_{rad} = 3.5$ K. For larger radial energies, the lifetime is dropping exponentially.

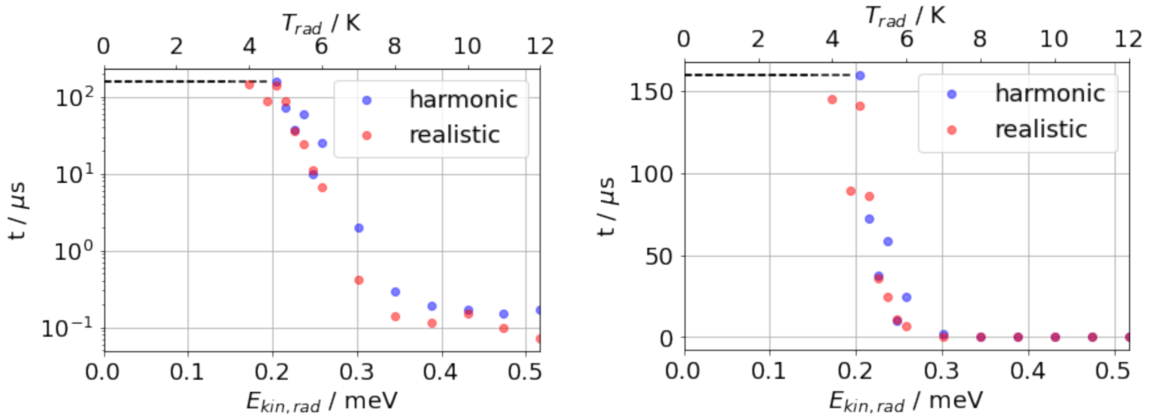

(a) (b)

Figure 4.17.: Lifetime of two-electron Coulomb crystal, measured for various radial energies in the realistic trap potential (red) and in the harmonic potential (blue). Figure a) uses a log scale, figure b) uses a linear scale. The dashed line marks the end of the simulation time at 160 μs.

Another scan is carried out to find the dependency of the crystal lifetime on the axial energy. Again, the results are averaged over three simulations. This time the radial initial energy is fixed at $T_{rad} = 0.4$ K. The axial initial energy in the stretch mode is varied. The temperature of the axial tank circuit $T_{res} = 0.4$ K is kept constant. The results are shown in figure 4.18, again for simulations of the realistic trap potential and the harmonic potential. Overall, the behavior is similar to that of the first scan. Obviously, the crystal is more sensitive to an increase of the axial stretch mode energy than to an increase of the radial zigzag mode energy. The crystal lifetime is in general smaller for the same kinetic energy. The crystal survives the whole 160 μs simulation only for low axial stretch mode energies below $T_{ax} = 1.5$ K. This is due to the potential strength, which is weaker in the axial direction than in the radial directions.

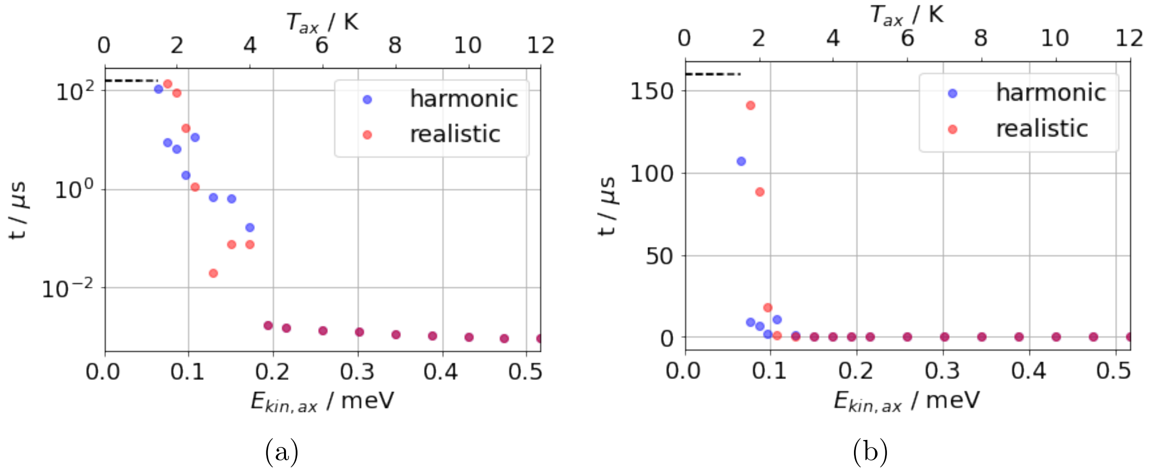

Figure 4.18.: Lifetime of two-electron Coulomb crystal, measured for various axial energies in the realistic trap potential (red) and in the harmonic potential (blue). Figure a) uses a log scale, figure b) uses a linear scale. The dashed line marks the end of the simulation time at 160 μs.

Overall, there is no systematic difference between the crystal stability in the realistic trapping potential in comparison to the approximated harmonic potential. For future investigations on this particular electron trap this means that it is sufficient to do calculations with the harmonic approximation. This saves a lot of effort and simulation time.

Still, some open questions remain. For high energies, the lifetime shown in the figure seems to be a quite accurate measurement. The fluctuations are low because the lifetime is not determined by the Boltzmann distribution of the axial energy, but only by the initial conditions. For low initial energies, the lifetime is determined by the Boltzmann distribution. A peak in the energy drives the switching of the electrons positions. To determine a reliable average lifetime for this noise-dominated regime, far more than three simulations on each initial energy are needed. Due to limited computation time, this could not be achieved within this thesis, but is a point of interest for future research. The same applies for simulation times longer than 160 μs. Simulations in the range of ms to s are of special interest for trapped electron experiments on two-qubit operations. The gate time of an electron two-qubit gate is estimated to be 2 μs as discussed in [1]. If we strive for a gate fidelity of 10^{-4}, crystal lifetimes of at least 20 ms are necessary. At least an order of magnitude should be added to the bare gate time for pre- and post-processing, which gives time scales of several hundreds of ms.

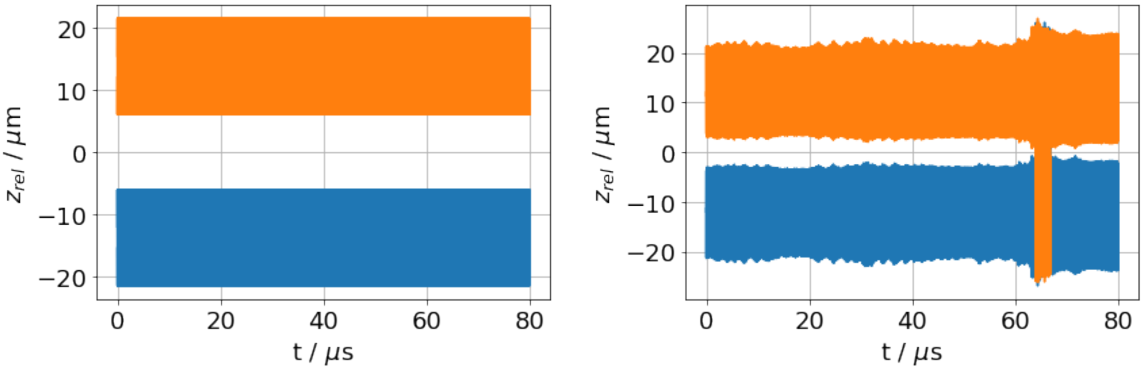

(a) (b)

Figure 4.19.: Relative z position of both electrons for simulations with initial radial energies of a) $T_{rad} = 0.4$ K and b) $T_{rad} = 5.5$ K in the realistic potential.

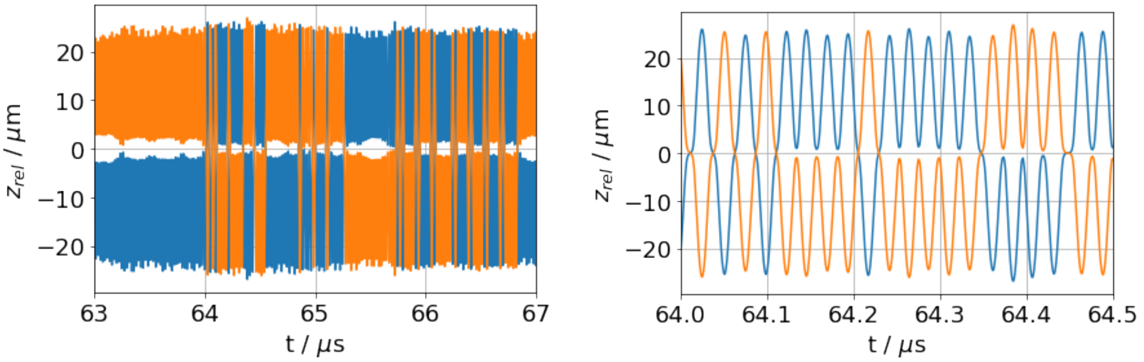

(a) (b)

Figure 4.20.: Relative z position of both electrons as they switch sides after 64 μs in the simulation with $T_{rad} = 5.5$ K. Figure a) shows the dynamics over a time period of 4 μs to give an overview, b) shows it over 0.5 μs to reveal more detail.

For additional visualisation on the dynamics of the two-electron crystal, figure 4.19 shows the relative z position of both electrons in the realistic trap potential for two different initial radial energies. A time period of 80 μs is covered. Both simulations are done with initial energy only in the relative motion with $T_{ax} = T_{res} = 0.4$ K. The left picture a) shows the dynamics of a very stable crystal, initialised with low radial energy $T_{rad} = 0.4$ K. Both electrons remain strictly within a very well-defined region. They come not even close to switching positions. The right picture b) shows the results of the same simulation with higher initial radial energy of $T_{rad} = 5.5$ K. With regard to figure 4.17, this corresponds to an unstable crystal. The energy is not high enough to break the crystal immediately, it survives a little more than 60 μs before the electrons switch positions due to a peak in the

Boltzmann distribution of axial energies. Also, within the first 60 μs the dynamics of the crystal is less uniform compared to the previous case. The electrons approach each other far more. The critical switching region after approximately 64 μs is depicted in greater detail in figure 4.20. Mostly, the electrons remain on one side of the center-of-mass for a couple of oscillation cycles, before they switch sides again.

5. Conclusion and Outlook

In this chapter, the thesis is summarized with respect to the research question of **numerical investigation of the dynamics and stability of electrons in a Paul trap**. Finally, a short outlook of potential further research is given.

Within the scope of this thesis, particle simulations of electrons were performed using the realistic potential of a 3-layer planar Paul trap. The trap is currently in use for experiments at the University of California Berkeley. It is designed for secular frequencies of $\omega_{rad} = 2\pi \cdot 300$ MHz and $\omega_{ax} = 2\pi \cdot 30$ MHz. The realistic potential of the trap was found numerically with a finite element algorithm, using the Ansys Electronics software. To create a continuous potential out of the grid points, the numerical data was fitted to an expansion of the trapping potential in spherical harmonics. As reference, a harmonic potential was used. To assure energy conservation, the particle simulation uses symplectic Velocity Verlet integration.

As a first test application of the simulation, the motional secular frequencies and first sideband frequencies of electrons in the trap were calculated. They match well with the theoretical predictions and the experimental observations.

A model for resistive cooling in axial direction and the associated Johnson Nyquist noise was introduced, implemented and tested. Key parameter of the model is the noise strength. It was determined empirically to match the experimental observation, i.e. an equilibrium temperature of the electron, equal to the resistors temperature. In this work it was $T_{res} = 0.4$ K. For the particular trapping potential the noise strength was found to be $\langle U_{noise}^2 \rangle = 4k_B T_{res} R \frac{C_{bw}}{dt}$ with the simulation time step dt and scaling factor $C_{bw} = 0.16$. The cooling time constant observed in the simulation lies in the range of $3 - 8$ μs with an average of 5.3 μs, which is close to the theoretical prediction of 7 μs. It would be interesting to measure the noise strength and cooling time in future experiments to compare them with the predictions made here. Further work using the simulation could focus on determining a more accurate cooling time constant by averaging over a larger number of simulations.

Another aspect investigated in this thesis is the coupling of axial and radial motional modes due to anharmonicities and Coulomb interaction. This is studied for the realistic potential in terms of energy transferred between the modes. It was found that no energy is exchanged between the axial and radial modes of a single electron. The same holds for a two-electron crystal. As a consequence, implicit cooling of the radial modes through direct axial cooling and vice versa is not possible. On the other hand, heating of a singled motional mode does not affect any of the other modes as well. The decoupling of the radial and axial motional modes, observed within this particular trap, does not necessarily hold for other Paul traps. In traps with a stronger impact of anharmonicities, the behavior might be different. Also, RF-heating of two electrons in the gas state was observed. This demonstrates the big advantage of the crystal state that prevents the system from RF-heating. The axial cooling does not overcome the heating. For future experiments on electron qubits, these observations imply that additional radial cooling is necessary. In fact, radial cooling circuits are already being discussed and will be implemented in future electron trap experiments. Radial cooling can be implemented in the simulation in future work, following the same principles as already discussed for axial cooling.

Finally, the dynamics and stability of two-electron Coulomb crystals, which is the simplest possible crystal structure, were studied. The frequencies of the zigzag and stretch mode were calculated. They match very well with the theoretical predictions. Also, the coupling between the axial center-of-mass mode and stretch mode were investigated. It was found that no energy is transferred between the modes. Since resistive cooling only affects the center-of-mass motion, this implies that an alternative method is needed to remove energy from the relative motion. One possibility is to merge two electrons into a crystal, that have already been cooled separately.

The stability of the crystal was tested by measuring its lifetime for various initial kinetic energies in the zigzag- and stretch mode, while the axial center-of-mass mode was following the Johnson Nyquist noise. For an initial stretch mode energy of 0.4 K, the crystal is surviving a 160 μs simulation for zigzag mode energies below 3.5 K. For higher energies the lifetime is dropping exponentially. Similarly, for an initial zigzag mode energy of 0.4 K the crystal is surviving 160 μs for stretch mode energies below 1.5 K. This implies, that the crystal is more sensitive to stretch mode energy than to zigzag mode energy.

No significant difference in the lifetime was found between the realistic trap potential and the harmonic potential. For further investigations on this trap the harmonic approximation of the potential is sufficiently accurate, which can save a lot of calculational resources.

Future simulations can extend the observation time up to 1 s, which is the time required for practical use in quantum computation. Furthermore, the lifetime should be determined with higher precision by averaging over more simulations. Also, the Johnson Nyquist noise in radial direction can be considered. The crystal stability can be investigated with respect to the center-of-mass mode, as for now only the energy in the relative motional modes was varied. Electron crystals are most likely experimentally implemented in Paul traps with higher motional frequencies, since they promise better stability. Concrete plans exist in the Berkeley Trapped Ions group about a trap with motional frequencies of $\omega_{rad} = 2\pi \cdot 1$ GHz and $\omega_{ax} = 300$ MHz. This trap is not yet designed and therefore could not be simulated within the work of this thesis. However, it might already be interesting to simulate a harmonic potential with these motional frequencies. Another point of interest is the simulation of larger Coulomb crystals, consisting of more than two electrons. In general, direct comparison with experimental results are needed, but this is still a long way to go. The simulation methods proposed within this thesis can support future trapped electron experiments by giving predictions and verifying the observed behavior.

6. Bibliography

[1] Q. Yu, A. M. Alonso, J. Caminiti, *et al.*, „Feasibility study of quantum computing using trapped electrons“, *Phys. Rev. A*, vol. 105, p. 022 420, 2 Feb. 2022. DOI: `10.1103/PhysRevA.105.022420`. [Online]. Available: `https://link.aps.org/doi/10.1103/PhysRevA.105.022420`.

[2] S. Earnshaw, *On the nature of the molecular forces which regulate the constitution of the luminferous ether.* transactions of the Cambridge Philosophical Society, 1842.

[3] G. Littich, „Electrostatic Control and Transport of Ions on a Planar Trap for Quantum Information Processing“, Master's Thesis, ETH Zürich and University of California, Berkeley, May 2011.

[4] D. Kienzler, *Trapped-ion physics lecture*, This script is built in many parts from the "Cavity QED and trapped ion physics" lecture script by J.P. Home, 2021.

[5] P. Wieburg, „A Linear Paul Trap for Ytterbium Ions“, Master's Thesis, Universität Hamburg, Apr. 2014.

[6] M. Knoop, *Paul traps*, University Lecture, 2015.

[7] C. E. Pearson, D. R. Leibrandt, W. S. Bakr, *et al.*, „Experimental investigation of planar ion traps“, *Physical Review A*, vol. 73, no. 3, Mar. 2006. DOI: `10.1103/physreva.73.032307`. [Online]. Available: `https://doi.org/10.1103%2Fphysreva.73.032307`.

[8] P. Tirler, „Readout Considerations for Trapped Electron Quantum Computing“, Master's Thesis, ETH Zürich and University of California, Berkeley, Oct. 2022.

[9] H. Morse P. Feshbach, *Methods of Theoretical Physics: I.* McGraw-Hill, 1953.

[10] K. Okada, M. Wada, T. Takayanagi, *et al.*, „Characterization of ion Coulomb crystals in a linear Paul trap“, en, *Phys. Rev. A*, vol. 81, no. 1, Jan. 2010.

[11] R. Blümel, C. Kappler, W. Quint, *et al.*, „Erratum: Chaos and order of laser-cooled ions in a Paul trap“, en, *Phys. Rev. A*, vol. 46, no. 12, p. 8034, Dec. 1992.

[12] M. W. van Mourik, P. Hrmo, L. Gerster, *et al.*, „Rf-induced heating dynamics of noncrystallized trapped ions“, en, *Phys. Rev. A (Coll. Park.)*, vol. 105, no. 3, Mar. 2022.

[13] H. Rohde, S. T. Gulde, C. F. Roos, *et al.*, „Sympathetic ground-state cooling and coherent manipulation with two-ion crystals“, *J. Opt. B Quantum Semiclassical Opt.*, vol. 3, no. 1, S34–S41, Feb. 2001.

[14] J. W. Emmert, M. Moore, and R. Blümel, „Prediction of a deterministic melting transition of two-ion crystals in a Paul trap“, en, *Phys. Rev. A*, vol. 48, no. 3, R1757–R1760, Sep. 1993.

[15] N. H. Hermnanspahn, „Das magnetische Moment des gebundenen Elektrons in wasserstoffartigem Kohlenstoff (C 5+)“, PhD thesis, Johannes Gutenberg Universität Mainz, Mainz, 1999.

[16] M. Brownnutt, M. Kumph, P. Rabl, *et al.*, „Ion-trap measurements of electric-field noise near surfaces“, Sep. 2014. arXiv: `1409.6572 [quant-ph]`.

7. Acknowledgements

First of all would I like to thank Prof. Dr. Ralf Schneider for the incredible supervision during my Master thesis, but also throughout my whole studies. Both your professional and personal support really were beyond compare. I'm more than grateful for your guidance, your patience and the countless lessons I have learned from you and within your group about different fields of physics and computational sciences.

I would also like to pay my special regards to Prof. Dr. Hartmut Häffner for the great opportunity to visit his group at the UC Berkeley as a Visiting Student Researcher and to participate in his exciting research. It has been an extremely enriching experience that I don't want to miss.

For proofreading this thesis I wish to thank Florian Wagner, the best cubicle neighbor I could ask for, and Friederike von Arnim, the best actual neighbor I could ask for. Both of you have furthermore been extremely encouraging friends during the work on my thesis and beyond.

To my boyfriend Johannes Johnke, it's hard to express the gratitude I feel for you. Without you by my side throughout the past years I wouldn't be the same person that I am now. Thank you for being the one I can always turn to, for giving me so much confidence, for inspiring me.

Finally I like to thank my dear parents for steadily supporting me in every possible way during my studies. I know that I can always rely on you.

A. Appendix

A.1. Spherical Harmonics Basis Functions

Table A.1 presents the spherical harmonics basis functions Y_j of the expansion 2.32 in Cartesian coordinates up to the order $l = 6$.

l	**m**	**j**	$\mathbf{Y_j(x, y, z)}$
0	0	1	1
1	0	2	z
	1	3	$-x$
	-1	4	$-y$
2	0	5	$-\frac{1}{2}\,x^2 - \frac{1}{2}\,y^2 + z^2$
	1	6	$-3\,xz$
	-1	7	$-3\,yz$
	2	8	$3\,x^2 - 3\,y^2$
	-2	9	$6\,xy$
3	0	10	$z^3 - \frac{3}{2}\left(x^2 + y^2\right)z$
	1	11	$\frac{3}{2}\,x^3 + \frac{3}{2}\,xy^2 - 6\,xz^2$
	-1	12	$\frac{3}{2}\,x^2y + \frac{3}{2}\,y^3 - 6\,yz^2$
	2	13	$15\left(x^2 - y^2\right)z$
	-2	14	$30\,xyz$
	3	15	$-15\,x^3 + 45\,xy^2$
	-3	16	$-45\,x^2y + 15\,y^3$
4	0	17	$\frac{3}{8}\,x^4 + \frac{3}{4}\,x^2y^2 + \frac{3}{8}\,y^4 + z^4 - 3\left(x^2 + y^2\right)z^2$
	1	18	$-10\,xz^3 + \frac{15}{2}\left(x^3 + xy^2\right)z$
	-1	19	$-10\,yz^3 + \frac{15}{2}\left(x^2y + y^3\right)z$

	2	20	$-\frac{15}{2}\,x^4+\frac{15}{2}\,y^4+45\left(x^2-y^2\right)z^2$
	-2	21	$-15\,x^3y-15\,xy^3+90\,xyz^2$
	3	22	$-105\left(x^3-3\,xy^2\right)z$
	-3	23	$-105\left(3\,x^2y-y^3\right)z$
	4	24	$105\,x^4-630\,x^2y^2+105\,y^4$
	-4	25	$420\,x^3y-420\,xy^3$
5	0	26	$z^5-5\left(x^2+y^2\right)z^3+\frac{15}{8}\left(x^4+2\,x^2y^2+y^4\right)z$
	1	27	$-\frac{15}{8}\,x^5-\frac{15}{4}\,x^3y^2-\frac{15}{8}\,xy^4-15\,xz^4+\frac{45}{2}\left(x^3+xy^2\right)z^2$
	-1	28	$-\frac{15}{8}\,x^4y-\frac{15}{4}\,x^2y^3-\frac{15}{8}\,y^5-15\,yz^4+\frac{45}{2}\left(x^2y+y^3\right)z^2$
	2	29	$105\left(x^2-y^2\right)z^3-\frac{105}{2}\left(x^4-y^4\right)z$
	-2	30	$210\,xyz^3-105\left(x^3y+xy^3\right)z$
	3	31	$\frac{105}{2}\,x^5-105\,x^3y^2-\frac{315}{2}\,xy^4-420\left(x^3-3\,xy^2\right)z^2$
	-3	32	$\frac{315}{2}\,x^4y+105\,x^2y^3-\frac{105}{2}\,y^5-420\left(3\,x^2y-y^3\right)z^2$
	4	33	$945\left(x^4-6\,x^2y^2+y^4\right)z$
	-4	34	$3780\left(x^3y-xy^3\right)z$
	5	35	$-945\,x^5+9450\,x^3y^2-4725\,xy^4$
	-5	36	$-4725\,x^4y+9450\,x^2y^3-945\,y^5$
6	0	37	$-\frac{5}{16}\,x^6-\frac{15}{16}\,x^4y^2-\frac{15}{16}\,x^2y^4-\frac{5}{16}\,y^6+z^6-\frac{15}{2}\left(x^2+y^2\right)z^4+\frac{45}{8}\left(x^4+2\,x^2y^2+y^4\right)z^2$
	1	38	$-21\,xz^5+\frac{105}{2}\left(x^3+xy^2\right)z^3-\frac{105}{8}\left(x^5+2\,x^3y^2+xy^4\right)z$
	-1	39	$-21\,yz^5+\frac{105}{2}\left(x^2y+y^3\right)z^3-\frac{105}{8}\left(x^4y+2\,x^2y^3+y^5\right)z$
	2	40	$\frac{105}{8}\,x^6+\frac{105}{8}\,x^4y^2-\frac{105}{8}\,x^2y^4-\frac{105}{8}\,y^6+210\left(x^2-y^2\right)z^4-210\left(x^4-y^4\right)z^2$
	-2	41	$\frac{105}{4}\,x^5y+\frac{105}{2}\,x^3y^3+\frac{105}{4}\,xy^5+420\,xyz^4-420\left(x^3y+xy^3\right)z^2$
	3	41	$-1260\left(x^3-3\,xy^2\right)z^3+\frac{945}{2}\left(x^5-2\,x^3y^2-3\,xy^4\right)z$
	-3	42	$-1260\left(3\,x^2y-y^3\right)z^3+\frac{945}{2}\left(3\,x^4y+2\,x^2y^3-y^5\right)z$
	4	42	$-\frac{945}{2}\,x^6+\frac{4725}{2}\,x^4y^2+\frac{4725}{2}\,x^2y^4-\frac{945}{2}\,y^6+4725\left(x^4-6\,x^2y^2+y^4\right)z^2$
	-4	44	$-1890\,x^5y+1890\,xy^5+18900\left(x^3y-xy^3\right)z^2$
	5	45	$-10395\left(x^5-10\,x^3y^2+5\,xy^4\right)z$
	-5	46	$-10395\left(5\,x^4y-10\,x^2y^3+y^5\right)z$
	6	47	$10395\,x^6-155925\,x^4y^2+155925\,x^2y^4-10395\,y^6$
	-6	48	$62370\,x^5y-207900\,x^3y^3+62370\,xy^5$

A.2. Expansion Coefficients for Two Layer Trap

The table A.2 shows the coefficients $M_{j,DC}$ and $M_{j,RF}$ of the spherical harmonics expansion of the DC- and RF- potential up to $l = 4$ or correspondingly $j = 25$. They were determined by fitting the potential data of the corresponding electrode configurations to the expansion. For better clarity the coefficients in the table are split into a number M_j / dp and it's decimal power dp. This provides an overview of the amount that each polynomial of the expansion contributes to the trapping potential. When reading the table it should be recognised that coefficients of order l are multiplied by a polynomial of order l, effectively increasing the decimal power dp by l. However it is visible that for both the static and the dynamic potential the higher order harmonics contribute less than the lower order harmonics. For each order l the most dominant values are highlighted in red. While for the DC-potential the quadratic polynomials of order $l = 2$ have a contribution of $10^{-7} \cdot 10^{2} = 10^{-5}$, the polynomials of order $l = 4$ have only a contribution of $10^{-13} \cdot 10^{4} = 10^{-9}$. Similarly for the RF-potential the quadratic polynomials of order $l = 2$ have a contribution of $10^{-7} \cdot 10^{2} = 10^{-5}$, the polynomials of order $l = 4$ have only a contribution of $10^{-14} \cdot 10^{4} = 10^{-10}$. This observation justifies to cut off the expansion after $l = 4$.

l	**j**	$\mathbf{M_{j,DC}}$ **/ dp**	**dp**
0	1	3.06	-02
1	2	2.3	-06
	3	-1.14	-04
	4	-1.14	-06
2	5	-9.57	-07
	6	-1.17	-08
	7	-1.96	-11
	8	1.34	-07
	9	-2.39	-09
3	10	8.35	-12
	11	-1.91	-11
	12	-1.37	-12
	13	2.18	-12
	14	-5.75	-14
	15	-4.19	-12
	16	-3.19	-13
4	17	1.61	-13
	18	8.83	-15
	19	8.42	-15
	20	-8.72	-14
	21	4.93	-15
	22	-8.61	-16
	23	1.38	-15
	24	-4.58	-15
	25	5.74	-16

l	**j**	$\mathbf{M_{j,RF}}$ **/ dp**	**dp**
0	1	8.07	-01
1	2	-3.72	-08
	3	1.44	-07
	4	3.42	-08
2	5	8.44	-10
	6	-4.88	-10
	7	5.26	-10
	8	-2.64	-07
	9	2.66	-10
3	10	-7.51	-12
	11	-7.46	-13
	12	2.43	-12
	13	-1.55	-13
	14	-2.33	-13
	15	-1.4	-12
	16	-2.75	-13
4	17	5.15	-14
	18	-4.34	-15
	19	-1.53	-14
	20	-2.21	-15
	21	-1.53	-15
	22	-1.67	-16
	23	-6.26	-16
	24	6.15	-15
	25	-2.51	-16

Table A.2.: Expansion coefficients $M_{j,DC}$ and $M_{j,RF}$ up to $l = 4$ found by fitting the numerical DC- and RF-potential to the spherical harmonics expansion. The dominant coefficients are marked in red.